A quantitative comparison of high latitude electric field models during a large geomagnetic storm

L. Orr[1,3], **A. Grocott**[1], **M.-T. Walach**[1], **G. Chisham**[2], **M.P. Freeman**[2], **M.M. Lam**[2], **R.M. Shore**[2]

[1]Space and Planetary Physics, Lancaster University
[2]British Antarctic Survey
[3]Now at British Geological Survey

Key Points:

- The Heelis model is hugely dependent on the transpolar voltage proxy used as input and when based on the Kp index it is very poor
- Models similar during quiet conditions but the spacecraft-based models are vastly different to the SuperDARN-based models during storm times
- As storm times are important for Joule Heating and satellite drag these differences must be considered by model users

Corresponding author: L.Orr, `lauren@bgs.ac.uk`

Abstract

Models of the high-latitude ionospheric electric field are commonly used to specify the magnetospheric forcing in thermosphere or whole atmosphere models. The use of decades-old models based on spacecraft data is still widespread. Currently the Heelis (Heelis et al., 1982) and Weimer (Weimer, 2005) climatology models are most commonly used but it is possible a more recent electric field model could improve forecasting functionality. Modern electric field models, derived from radar data, have been developed to incorporate advances in data availability (Thomas & Shepherd, 2018; Walach et al., 2022; Bristow et al., 2022). It is expected that climotologies based on this larger and up-to-date dataset will better represent the high latitude ionosphere and improve forecasting abilities. An example of two such models, which have been developed using line-of-sight velocity measurements from the Super Dual Auroral Radar Network (SuperDARN) are the Thomas and Shepherd model (TS18) (Thomas & Shepherd, 2018), and the Time-Variable Ionospheric Electric Field model (TiVIE) (Walach & Grocott, 2022). Here we compare the outputs of these electric field models during the September 2017 storm, covering a range of solar wind and interplanetary magnetic field (IMF) conditions. We explore the relationships between the IMF conditions and the model output parameters such as transpolar voltage, the polar cap size and the lower latitude boundary of convection. We find that the electric potential and field parameters from the spacecraft-based models have a significantly higher magnitude than the SuperDARN-based models. We discuss the similarities and differences in topology and magnitude for each model.

Plain Language Summary

To prevent collisions between satellites and space junk within the Earth's space environment we need to accurately predict their position. The Ionosphere is part of the upper atmosphere of the Earth a which is affected by space weather events such as geomagnetic storms. Accurate ionospheric electric field models are key to accurate orbit prediction. Currently the use of decades-old models based on spacecraft data from the 80s is still widespread. We aim to compare the output from these commonly used spacecraft-based models to more recent models which were developed using line-of-sight velocity measurements from the Super Dual Auroral Radar Network (SuperDARN). We find that the parameters output from the spacecraft-based models often are significantly different to the SuperDARN-based models. We discuss the similarities and differences in topology and magnitude for each model.

1 Introduction

The high latitude ionospheric electric field is driven by coupling of the solar wind, magnetosphere and ionosphere. It is an integral part of space weather and can affect both ground-based and space-born technology; it is therefore important that we can accurately model the ionospheric electric field. For example, the ionospheric electric field is an important source of uncertainty in satellite drag and hence the risk of collisions between satellites and space debris. The electric field causes ions and electrons to accelerate parallel to the electric field and drift perpendicular to it such that they collide with neutral particles and heat the thermosphere. This Joule heating expands the thermosphere, causing the air density to locally increase and hence satellite drag.

One impact of the Space Weather Instrumentation, Measurement, Modelling and Risk: Thermosphere (SWIMMR-T) programme aims to improve the UK's ability to specify and forecast the thermosphere. To do this, it is using and developing a physics-based, coupled thermosphere-ionosphere assimilative model for satellite drag and other applications called AENeAS (Advanced Ensemble electron density [Ne] Assimilation System) (Elvidge & Angling, 2019). AENeAS is based on the Thermosphere Ionosphere Electrodynamics General Circulation Model (TIEGCM (Dickinson et al., 1981)) which requires

an appropriate ionospheric electric field model of which there are many models currently used routinely in space physics. Heelis et al. (1982) and Weimer (2005) are two climatological models based on spacecraft data that are commonly used in modern atmospheric and space weather models. Currently TIEGCM and hence AENeAS interchangeably uses either a version of the Heelis et al. (1982) model, similar to that from M. Hairston and Heelis (1990), or the Weimer (2005) model but it is possible that a 'state-of-the-art' electric field model will improve its functionality. Similarly, the Whole Atmosphere Community Climate Model With Thermosphere and Ionosphere Extension (WACCM-X) (Liu et al., 2018), is another General Circulation Model (GCM) which currently uses Heelis to specify the electric field patterns, but Liu et al. (2018) suggests that the use of Weimer (2005) or data assimilative schemes (Richmond & Kamide, 1988) would improve its simulations.

The Super Dual Auroral Radar Network (SuperDARN) (Chisham et al., 2007), a collection of ground-based coherent scatter radars, has been used for many years to measure and model ionospheric convection (Ruohoniemi & Baker, 1998). The addition of SuperDARN-based models could potentially help improve TIEGCM, AENeAS, WACCM-X and other modern GCMs by having an ionosphere model based on a spatially and temporally well sampled dataset from the most recent solar cycle.

Table 1 summarises the Heelis, Weimer, and SuperDARN family of models and highlights the similarities and differences between them. An important difference is the time interval of data on which each model is based, which is illustrated in Figure 1 in relation to the solar cycle and sunspot number. Figure 1 plots the previous four solar cycles (SC21-24) with shading showing the time range over which each of the models were devised. Weimer (2005) and M. Hairston and Heelis (1990), denoted W05 and HH90 respectively, cover the 20 month period in the declining phase of SC21 for which Dynamics Explorer 2 (DE-2) was active. Ruohoniemi and Greenwald (1996) (RG96) covered most of SC22, Pettigrew et al. (2010) (PSR10) most of of SC23, Cousins and Shepherd (2010) (CS10) the majority of SC23 and Thomas and Shepherd (2018) (TS18) and Walach and Grocott (2022) (TiVIE) most of SC24.
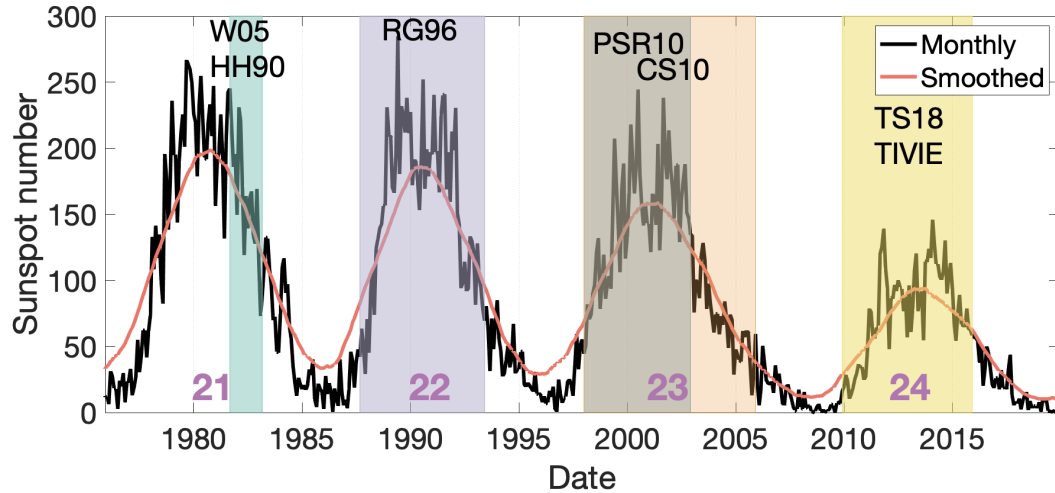
Figure 1. Monthly mean total sunspot number with W05, HH90, RG96, PSR10, CS10 and TS18 time spans.

Heelis et al. (1982) was originally a purely mathematical model for high latitude ionospheric convection based on Volland (1975). This model takes input parameters such

as the radius of the convection reversal boundary, the longitude of the dayside and night-side zero potential lines, and the magnitude of the maximum and minimum electric potentials. The full list of input variables are specified in section 1, Supplementary Information (SI).

This model was further developed by M. Hairston and Heelis (1990) such that the convection pattern was parameterised by the Interplanetary Magnetic Field (IMF) B_y and the transpolar voltage, Φ_{PC}, only. They used data from DE-2, which operated between August 1981 and March 1983 in a polar orbit at altitudes of 300-1000km, to find relationships between the parameters in Heelis et al. (1982) with B_y and Φ_{PC}. The DE-2 passes used in this analysis were limited to those starting and ending within 3 hours of magnetic local time (MLT) of the dawn-dusk meridian during intervals with IMF B_z negative. Fewer than 100 passes fulfilled those criteria.

ID	Reference	Time span	Solar cycle	Data source	Para-meters	Grid	Lower boundary
H82	Heelis 1982				See tbl. S1, SI	Analytical.	Equator.
HH90	Hairston & Heelis 1990	08/1981 - 03/1983 (< 100 passes)	SC21 (max. - declining phase)	DE-2	Φ_{PC}, B_y. $-B_z$ only	Analytical, continuous, offset polar cap	Equator.
W05	Weimer 2005	08/1981 - 03/1983 (2064 passes)	SC21 (max. - declining phase)	DE-2	B_y, B_z, n, V, tilt	Define N bands of width $D = \frac{R}{60}$. For radius $\frac{R}{D} \leq 26$, do SH cap fit. For $26 < \frac{R}{D} \leq 60$, do azimuthal Fourier expansions per band.	4.2° offset circle with radius $R = f(\theta, B_{yz}, V, n)$.
TS18	Thomas & Shepherd 2018	2010-2016	SC24 (min. - declining phase)	Super-DARN (SD)	E_{sw}, θ_{clk}, tilt	SH cap fit where cap size is circle whose lowest latitude equals HMB.	Min. latitude HMB with max. midnight latitude for merged vectors with $V > 150$ m/s for 25+ points adjacent to boundary.
TS18 Kp	Thomas & Shepherd 2018	2010-2016	As above	SD	Kp, θ_{clk}	As above	As above
TiVIE (mode 3)	Walach et al 2022	54 storms 2010-2016	As above	SD	Storm Phase: Sym-H	As above	The lower quartile (25%) of the HMBs from the original maps is used.

Table 1. List of commonly used electric field models with details summarised.

The Weimer model (Weimer, 2005) (W05) is a statistical electric potential model of the high-latitude ionosphere. Measurements of the ionospheric electric field from more than 2600 passes of the DE-2 satellite were used alongside solar wind and IMF conditions to create an empirical model of potential patterns. The model was developed from measurements of the electric potential variation along the satellite path estimated from the integration of electric field components in the direction of motion. This model has been updated a number of times to increase spacecraft resolution, with the low-latitude boundary varying and improving the representation of the potentials using a combination of Fourier series and spherical harmonics (Weimer, 1995, 1996, 2001, 2005). Input parameters include the IMF B_y and B_z components, the dipole tilt angle of the Earth, the solar wind velocity V, and the plasma number density n. Electric potential is calculated at different points in geomagnetic latitude and magnetic local time (MLT), in AACGM (Altitude Adjusted Corrected Geomagnetic) coordinates. Weimer (2005) defines 60 latitude bands then uses spherical harmonics to describe the potentials within the highest 26 bands around the offset pole. Fourier series as a function of angular position (and parameters) are used to represent the potentials in the lower 34 latitude bands.

Ruohoniemi and Greenwald (1996) were first to use line-of-sight $E \times B$ velocity measurements from SuperDARN to derive a set of statistical electric potential patterns organized by IMF magnitude and clock angle. This 'climatological' model was primarily built to augment instantaneous SuperDARN measurements in the SuperDARN fitting procedure known as Map Potential (Ruohoniemi & Baker, 1998). Map Potential uses all available SuperDARN line-of-sight velocity data at a given time to derive an instantaneous spherical harmonic solution of the electrostatic potential that is constrained by the statistical model in regions of no data coverage. Consequently the Map Potential solution tends towards the instantaneous measured data where it exists and towards the climatological model where the measurements are missing. Pettigrew et al. (2010) improved the climatological model by adding dipole tilt angle as a parameter and Cousins and Shepherd (2010) expanded the dataset and added a dependence on solar wind velocity. Recently Thomas and Shepherd (2018) developed this model further using data from solar cycle 24, which exploited the expansion of SuperDARN radars to mid-latitudes ($50 - 60°$) and to the polar cap ($80 - 90°$). Their climatological electric potential patterns were organized by the solar wind electric field magnitude (E_{sw}), the IMF clock angle (θ_{clk}), and the dipole tilt angle. This is the model version currently used in Map Potential. Thomas and Shepherd (2018) further included a version of their climatology parameterised by the magnetic planetary 'Kp' index and clock angle.

A more recent model that can be used to improve ionospheric electric field representation within atmosphere modelling is the Time-Variable Ionospheric Electric field (TiVIE) model (Walach & Grocott, 2022). Unlike previous SuperDARN-based models, which are based on instantaneous climatologies, TiVIE makes use of novel parameterisations to capture major sources of time-variability in the electric field pattern. TiVIE combines SuperDARN data into superposed epoch analyses to model the electric field using spherical harmonics for different time-varying scenarios via one of three modes. Mode 1 is directly related to the upstream solar wind conditions of the IMF, parameterised by IMF strength bins, clock angle and a solar wind steadiness timescale. This latter parameter allows for differences in the duration of a given state of solar wind driving to be captured. Mode 2 is a substorm mode, and may be parameterised by the universal time, magnetic latitude and local time, of a substorm onset. This allows for variability due to the substorm, that may be temporaly decoupled from the solar wind driver, to be captured. Mode 3 parameterises the electric field by storm phase using Sym-H to account for the variability introduced specifically by geomagnetic storms. This mode is based on a list of 54 storms from 2010-2016 (Walach & Grocott, 2019; Walach et al., 2021). Geomagnetic storms are a major source of variability that is not captured using instantaneous IMF parameterisations. Instead of the instantaneous IMF, the mode 3 model uses the normalised time within the initial, main, and recovery phases defined using the Sym-H

162 index. SuperDARN measurements at each normalised time are then averaged over all
163 storms to estimate the electric potential by a spherical harmonic fit.

164 In this paper we will quantitatively compare the aforementioned ionospheric elec-
165 tric field models (HH90, W05, TS18, and TiVIE) for the 7th-8th September 2017 geo-
166 magnetic storm. Choosing a storm interval allows us to test the models under extreme
167 driving conditions when space weather impacts will be greatest and when we might ex-
168 pect the models to be most deficient and diverse due to their limited input dataset. It
169 also enables us to contrast models based on typical data with the storm mode of the TiVIE
170 model that is specifically tailored to storm times. Although we have chosen a single event,
171 the storm we have picked nonetheless encompasses a variety of solar wind driving con-
172 ditions and thus a range of input parameterisation to the models, and there is good Su-
173 perDARN data coverage throughout the main phase of the storm. Performing an event-
174 based comparison, rather than a statistical study avoids the complication introduced by
175 the models having different input parameters (see Table 1). For example, TS18 is pa-
176 rameterised by solar wind electric field E_{sw} and clock angle θ_{clk}, whereas W05 is param-
177 eterised by solar wind speed V and IMF B_y and B_z components. Consequently, the TS18
178 and W05 statistical model outputs cannot be uniquely compared because a given E_{sw}
179 and θ_{clk} state can in general arise from different combinations of V, B_y, and B_z, whereas
180 a given event naturally selects all parameter values. Event-based comparison also allows
181 us to compare the model outputs to the SuperDARN Map Potential output as a "ground-
182 truth" dataset, recognising that we are comparing this "ground-truth" to both Super-
183 DARN and non-SuperDARN models.

184 In section 2 we describe the method, the model versions and the data used, sec-
185 tion 3 shows the results and section 4 discusses the findings.

2 Methods

2.1 Model versions

188 The models used in this study are summarised in Table 1. The version of the Heelis
189 model used for the analysis in this paper is taken from TIEGCM (Qian et al., 2014) within
190 AENeAS (Elvidge & Angling, 2019; HAO, 2018). A full description of the code is included
191 in the SI but we will refer to it as HH90 due to its similarities with M. Hairston and Heelis
192 (1990). The W05 model is described by Weimer (2005) and was provided by Daniel Weimer.
193 TS18 (Thomas & Shepherd, 2018) is available as part of the Radar Software Toolkit (RST
194 (4.4.1)) (SuperDARN Data Analysis Working Group et al., 2021). TiVIE refers to the
195 geomagnetic storm (mode 3) version.

2.2 Selection of event

197 The chosen interval of interest is from 20:00 UT on September 7th to 03:20 UT on
198 September 8th. The interval is within a geomagnetic storm, as shown in Figure 1 of the
199 Supplementary Information by the characteristic rapid decrease in the Sym-H index and
200 slow recovery. The minimum Sym-H is -146 nT, which defines this event as an intense
201 storm (-250 nT < minimum Sym-H < -100 nT).

202 Following the definition of storm phases devised by Walach and Grocott (2019) for
203 mode 3 of the TiVIE model, the storm begins at 11:02 UT on 7th September and ends
204 at 18:40 UT on 10th September. Within this, the storm's initial phase is from 11:02 to
205 23:07 UT on 7th September, the main phase then follows until 01:08 UT on 8th Septem-
206 ber, and thereafter the recovery phase until the storm end at 18:40 UT on 10th Septem-
207 ber. It should be noted that the Walach and Grocott (2019) definition of the start of a
208 storm is not based on the Sudden Storm Commencement (SSC), as is commonly the case.
209 Instead, it is the start of a storm initial phase that is defined as a quiet interval ahead

of the storm main phase in which Sym-H maximises and is greater than -15 nT. The Walach and Grocott definition is more practical for storms without an SSC or due to the interaction of multiple solar ejecta, as is the case in this storm (Dimmock et al., 2019). The 7 hour 20 minute interval within the storm has been selected to include the 2 hour 3 minute main phase from 23:07 UT (7th) to 01:10 UT (8th) and similar length intervals of the surrounding initial and recovery phases.

2.3 Model input control variables

As mentioned in the Introduction, the decision to use a single event to compare the models is because they each have different control variables as input (see Table 1) which cannot be uniquely related to each other. For example, (i) TS18 has 120 climatological patterns for different combinations of inputs E_{sw}, θ_{clk}, and dipole tilt angle (where $E_{SW} = |V_x|\sqrt{B_y^2 + B_z^2}$ and $\theta_{clk} = \arctan(\frac{B_y}{B_z})$), (ii) W05 input control variables includes IMF B_y, B_z, the dipole tilt angle of the Earth, solar wind velocity, V, and plasma number density, n. (iii) HH90 takes Φ_{PC} and IMF B_y as input control variables, and (iv) TiVIE mode 3 uses only storm phase and normalised time within it.

Considering first TiVIE mode 3, the ionospheric electric field is defined in this model for each time step within the initial, main, and recovery phases at 2 minutes cadence. The duration of these phases are defined in the model to be 587, 272, and 1673 time steps, respectively, corresponding to the average length in minutes of these phases for the 54 storms on which the model is based. For the September 2017 storm event studied here, the duration of the initial, main and recovery phases are found to be 725, 121, and 3932 min, respectively. Thus the model time step in each phase is scaled by the ratio of the event phase duration to the model phase duration, i.e., 725/587 = 1.24 min, 121/272 = 0.445 min, and 3932/1673 = 2.35 min for the initial, main , and recovery phases, respectively. Consequently, for the interval of interest from 20:00 UT on 7 September to 03:20 UT on 8 September, we use the final 151 of the 587 time steps of the model initial phase, all 272 time steps of the model main phase, and the first 57 of the 1673 time steps of the model recovery phase, making a total of 480 model time steps.

For the W05 and TS18 models, the interplanetary input control variables are provided by, or derived from, measurements from the ACE (Advanced Composition Explorer) and WIND spacecraft in the OMNI dataset of the NASA Geophysical Data Center `http://omniweb.gsfc.nasa.gov/ow.html`. The measurements have been averaged at one minute cadence such that the time interval of interest has 441 time points. They have been time lagged to the bow shock nose using methods specific to the spacecraft (Farris & Russell, 1994; Shue et al., 1997). A further time lag is added from the bow shock to the magnetopause based on an estimation of the subsolar magnetosheath transit time from (Khan & Cowley, 1999).

In the HH90 model, the input control variables are IMF B_y, which is available from OMNI, and the transpolar cap voltage Phi_{PC}, which is a property of the ionospheric electric field (see section 2.4) and hence usually a model output variable. Therefore we need an equation to relate Φ_{PC} to IMF and solar wind conditions, or other OMNI measurements. Five such equations are listed below:

Lockwood Equation

Lockwood and McWilliams (2021) recently used more than 65,000 hourly averages of Φ_{PC} determined from over 25 years of SuperDARN radar observations to estimate the 'optimum' solar wind-magnetosphere coupling function.

$$\Phi_L = B_{YZ}^{0.64} \rho_{SW}^{0.02} V_{SW}^{0.55} \sin^{2.5}(\theta_{clk}/2) \tag{1}$$

where B_{YZ} is the transverse component of the interplanetary magnetic field, perpendicular to the Sun-Earth line. ρ_{SW} is the mass density, V_{SW} the solar wind speed, and θ_{clk}

is the clock angle (Lockwood & McWilliams, 2021). Each of these parameters are available at 1 minute resolution at the bow shock from OMNI, hence Φ_L can be calculated at 1 minute cadence, with the lag from the bow shock nose to the magnetosphere added.

Kp

The equation currently used within TIEGCM and AENeAS (HAO, 2018) is a relationship with Kp. This is a 3-hr index provided as part of the Low Resolution OMNI (LRO) data set by the German Research Centre for Geosciences (GFZ, Potsdam).

$$\Phi_{Kp} = 15 + 15Kp + 0.8Kp^2 \tag{2}$$

An obvious problem with this estimation is that the K_p index has a cadence of 3 hours and therefore Φ_{Kp} does not capture smaller-scale temporal variations. Kp values are supplied every 3 hours, beginning at midnight, and we will use the most up-to-date Kp value at each subsequent time step. Unlike solar wind data which is measured upstream, Kp is not well forecast so is not as useful for a forecasting model. A simplified version of this equation appears in Boyle et al. (1997). According to Boyle et al. (1997) Kp provides a reasonable estimate of Φ_{PC} if the IMF has been steady for several hours.

Polar Cap Index

Ridley and Kihn (2004) show a seasonal trend in the relationship between the Polar Cap Index (PCI) and transpolar voltage, and define a proxy Φ_{PCI}:

$$\Phi_{PCI} = 19.28 - 3.31\sin(T + 1.49) + 17.81 PCI, \tag{3}$$

$$T = (month - 1) \times 2\pi/12 \tag{4}$$

where *month* is the month of the year (i.e. January is *month*=1) and PCI is available as OMNI data. Therefore, this equation is directly comparable to the TS18 and W05 models. It is available at a 1-min cadence but like Kp it is not available in advance, so can not be used for forecasting.

Boyle Equation

$$\Phi_B = 10^{-4}V^2 + 11.7B\sin^3(\theta_{clk}/2) \tag{5}$$

which is defined such that Φ_B is the transpolar voltage in kV, V is the solar wind bulk velocity in km/s, B is the IMF magnitude in nT and θ_{clk} is the IMF clock angle (Boyle et al., 1997).

Milan Equation

$$\Phi_D = L_{eff}(V_x)V_x B_{YZ} \sin^{9/2}\frac{1}{2}\theta_{clk}, \tag{6}$$

$$L_{eff}(V_x) = 3.8\left(\frac{V_x}{4 \times 10^5}\right)^{1/3} \tag{7}$$

where Φ_D is the dayside reconnection rate, V_x is the solar wind speed and B_{YZ} is the magnitude of the projection of the IMF vector in the $Y - Z$ GSM plane(Milan et al., 2012).

Some studies have used Φ_{PC} as a proxy for dayside reconnection rate (Grocott et al., 2009; P. H. Reiff et al., 1981; P. Reiff et al., 1985). Milan et al. (2012) suggests two flaws in this method. 1) Viscous interaction of the solar wind and the magnetosphere can cause convection without dayside reconnection. 2) The relationship between the two parameters is complex. The intervals used in Milan et al. (2012) had good representation of all clock-angles and values of B_{YZ} up to 12 nT and solar wind dynamic pressure up to 12 nPa, but few beyond. One issue identified in our results below is very high values of Φ_D during storm time intervals.

2.4 Model output metrics

To quantitatively compare the models we produce time series of various model metrics that can be extracted from the modelled electric potentials as follows:

The transpolar voltage

$$\Phi_{PC} = \Phi_{max} - \Phi_{min}, \tag{8}$$

where Φ_{min} and Φ_{max} are the minimum and maximum electric potentials, respectively. We note that this may not represent the true transpolar voltage if the maximum and minimum potentials are not located at the foci of the dawn and dusk Dungey-cycle convection cells, respectively.

The polar cap residual

$$\Phi_{res} = \Phi_{max} + \Phi_{min} \tag{9}$$

These two equations provide measures of the strength of the convection and the asymmetry between the dawn and dusk convection cells, respectively.

Mean polar electric field

The mean electric field magnitude, $|\bar{EF}|$, above $60°$ magnetic latitude, measured in mV/m.

$$|\bar{EF}| = \sum_{\theta, \psi} \frac{|EF|}{N}, \tag{10}$$

where $\theta \geq 60°$ represents the Altitude Adjusted Corrected GeoMagnetic (AACGM-v2) latitude, ψ represents all magnetic longitudes, and N is the number of points. This metric is the mean electric field magnitude above $60°$ magnetic latitude, measured in mV/m. It allows us to include a measure of the mean strength of the convection for HH90, where Φ_{PC} is an input and thus contains limited information about the model performance.

The electric field is calculated using code adapted from part of the Heppner-Maynard-Rich Electric Field Model 1990 (J. P. Heppner, 1977; J. Heppner & Maynard, 1987; Rich & Maynard, 1989). The north-south component of the electric field is calculated at a point, Φ_i, by taking the difference of the potential at the point to the north, Φ_{i+1}, and the potential at the point to the south, Φ_{i-1}, divided by the geographic distance between the two points. The east-west component of the electric field is found in the same way by taking the gradient between a point to the east and west of a point in geographical coordinates.

Polar cap radius

A proxy for the radius of the polar cap, r_{pc}, is given by

$$r_{pc} = \frac{1}{2}(\theta_{max} + \theta_{min}) \tag{11}$$

where θ_{max} is the colatitude of the location of maximum potential and θ_{min} is the colatitude of the location of minimum potential. This measure is a proxy for the radius of the polar cap, with the same caveats as for the transpolar potential.

Low latitude boundary

A 'Heppner-Maynard boundary' (HMB) is routinely determined for all SuperDARN models as the lower-latitude limit of the convection (see table 1). The latitude of this boundary at midnight magnetic local time is specified when performing the spherical harmonic fit. In W05, the low latitude boundary (LLB) is defined by an offset circle (Weimer, 2005). In HH90 there is no LLB. Instead, equatorward of the polar cap boundary, the HH90 electric potential is described by a function that decreases exponentially with decreasing latitude (M. Hairston & Heelis, 1990). For purposes of comparison we will de-

337 fine the HH90 LLB as the latitude across which the mean electric potential drops be-
338 low 0.418 kV, which is the mean electric potential of the LLB for W05 throughout the
339 time period 7th September 20:00 UT to September 8th 03:20 UT.

3 Results

3.1 Parameterised time series of the September 2017 storm

342   In Figure 2 we present a quantitative comparison of convection pattern parame-
343 ters produced by the different models for a time period from 20:00 UT on the 7th to 03:20 UT
344 on the 8th September 2017, allowing for a range of IMF conditions during the initial,
345 main and recovery phases of the storm. The start and end times of the main phase, as
346 found from Sym-H using the method of Walach and Grocott (2019), are shown by the
347 vertical, dashed grey lines at 23:07 UT on 7th and 01:08 UT on 8th September. The pa-
348 rameters in figure 2 are listed in section 2.4. The vertical, dashed blue lines correspond
349 to the snapshots in figure 3.

350   Panel A shows the IMF parameters B_y and B_z in blue and orange, respectively.
351 The horizontal, dashed line indicates 0 nT. The time interval chosen displays a range of
352 IMF conditions, with positive and negative B_y and B_z plus a range of IMF clock angles.
353 Panel B shows the Sym-H index which is used to define the storm phases (vertical, grey
354 lines) as mentioned above. Panel C shows the number of SuperDARN vectors that were
355 available at each time point, included to identify to what extent the Map Potential is
356 relying on the TS18 model to infill the data gaps. The line-of-sight vectors are combined
357 into cells of an equal area polar grid of spatial resolution $\sim 110 \times 110$ km. The num-
358 ber of vectors are then the number of these gridded cells which are occupied by line-of-
359 sight vectors. When the number of available vectors is low, Map Potential relies on TS18
360 to fill the data gaps. The number of vectors is low throughout the initial phase but in-
361 creases to ~ 500 vectors through the peak of the storm.

362   Panel D shows the transpolar voltage proxies from subsection 2.3 equations 1 to
363 7. Through the initial phase, whilst IMF $B_z > \sim -10$ nT, all five proxies perform sim-
364 ilarly with values between 100 and 180 kV. When B_z drops further the IMF and solar
365 wind based proxies, Φ_B and Φ_D (equations 5 and 7), reach huge values of 416 kV and
366 631 kV respectively. Φ_L (equation 1) has a more conservative but still high value of 337 kV.
367 The PCI proxy, Φ_{PCI} (equation 4) reaches 306 kV, while the Kp proxy, Φ_{Kp} (equation
368 2) only reaches 186 kV; Kp is a three-hourly index and so lacks the higher-resolution de-
369 tail that is observed in the other three proxies that use 1-minute IMF data. In the fol-
370 lowing panels E-H we use the proxies Φ_L (equation 3) and Φ_{Kp} (equation 2) as the Φ_{PC}
371 input for HH90.

372   Panel E shows the transpolar voltage, Φ_{PC}, the difference between the maximum
373 and minimum electric potentialx (equation 8) for TiVIE, TS18, W05 and Map Poten-
374 tial, as well as the Φ_L and Φ_{Kp} proxies used in HH90. Considering first the spacecraft-
375 based models, HH90 (Φ_L) follows a similar trend to W05 throughout the storm but reaches
376 a higher peak of 337 kV at 23:38 UT on the 7th compared to 256 kV for W05. HH90 (Φ_{Kp})
377 remains relatively steady at 180-190 kV throughout the main phase and for 2 hours be-
378 fore and after it, due to its low 3-hour resolution as already noted in reference to panel
379 D. For the SuperDARN-based models Φ_{PC} is significantly lower. The TiVIE values are
380 elevated throughout the main phase, maximising at 141 kV. TS18 saturates at ~ 90 kV
381 when $B_z = -7$ nT from $\sim$20:50 UT and does not change significantly when IMF B_z con-
382 tinues to decrease. This is because the model is at its maximum E_{sw} bin where the model
383 electric potential is averaged over all $E_{sw} > 3$ mV/m. The Map Potential variation lies
384 between TiVIE and TS18. It shows more variation than TS18 and reaches a higher max-
385 imum of 124 kV. Map potential tends towards the TS18 model when the number of vec-
386 tors is low as the model increasingly relies on the TS18 background model to infill data
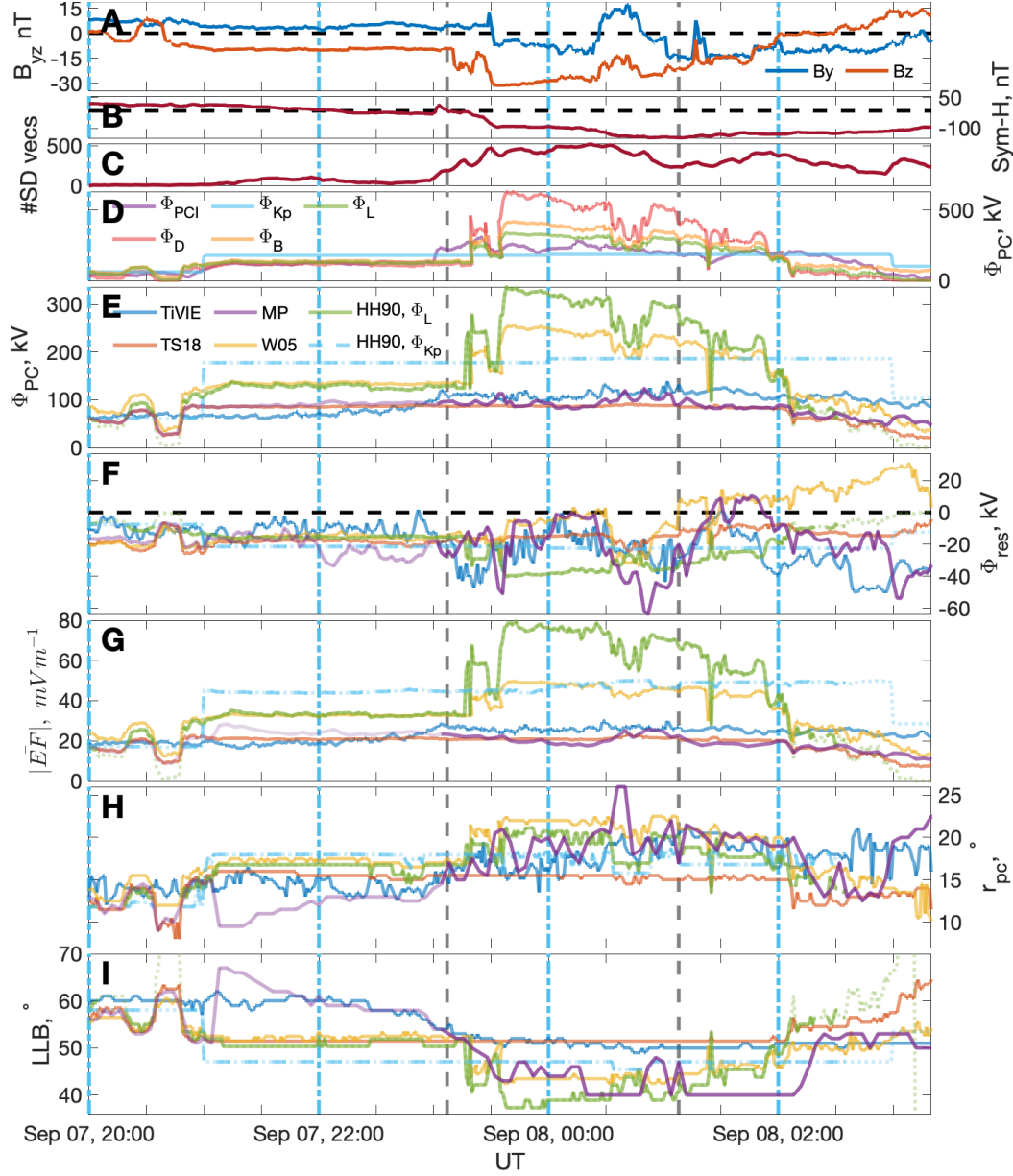
Figure 2. Panel A shows B_y (blue) and B_z (orange), panel B shows Sym-H, panel C the number of SuperDARN vectors available for the Map Potential, panel D shows five proxies for transpolar voltage, Φ_{PC} which are given as equations 2-7. Panel E plots the model outputs for Φ_{PC} from TiVIE, TS18, W05 and Map Potential. The models are each represented by the same set of colours in Panels D-I Where Map Potential is calculated from < 100 vectors it is plotted in lighter purple. Panel F shows Φ_{res} for the models as in equation 9. Panel G shows the mean electric field above $60°$ as calculated using equation 10. Panel H and I shows a proxy for the size of the polar cap and lower latitude boundary (LLB) per model, respectively as calculated in section 2.4. Vertical dashed grey lines represent the start and end of the main phase. Vertical dashed blue lines match the snapshots from figure 3.

387 gaps. When there are few SuperDARN vector measurements available (< 100), the Map
388 Potential parameter is shown in a lighter shade of purple.

Panel F is the residual of the potential, the sum of the maximum and minimum potential (equation 9), which we use as a measure of asymmetry between the dawn and dusk cells. If $\Phi_{res} < 0$, the dusk cell has a stronger magnitude whilst if $\Phi_{res} > 0$ the dawn cell is stronger. Through the main phase of the storm the dusk cell (Φ_{min}) is stronger than the dawn cell (Φ_{max}) for all models. Map Potential shows the highest asymmetry of any model towards the end of the main phase with $\Phi_{res} = -64 \, \text{kV}$ at 00:52 UT on the 8th. During the recovery phase the W05 model has $\Phi_{res} > 0$, meaning the dawn cell has a higher magnitude. This can be seen in figure 3 at 02:00 UT where $\Phi_{min} = -73.1 \, \text{kV}$ and $\Phi_{max} = 81.7 \, \text{kV}$.

Panel G shows the mean electric field vector magnitude $|\bar{EF}|$ of all vectors above $60°$ magnetic latitude (equation 10). The method for calculating electric fields from electric potential data is described in section 2.4. Trends in the time series are largely similar to those seen in panel E for Φ_{PC} but calculating a parameter from a range of latitudes and longitudes allows us to include the HH90 response in the comparison. HH90 (Φ_L) has a similar $|\bar{EF}|$ to W05 until 23:15 UT on the 7th September, with both having $|\bar{EF}| \sim 35 \, \text{mV/m}$. From 23:15 UT the HH90 (Φ_L) parameter increases sharply to maximise with $|\bar{EF}| \sim 80 \, \text{mV/m}$, approximately 160% of the maximum value of the W05 model. HH90 (Φ_{Kp}) has $|\bar{EF}| \sim 50 \, \text{mV/m}$ from shortly after 21:00 UT on the 7th until after 03:00 UT on the 8th. This is higher than the rest of the models until 23:15 UT when the $|\bar{EF}|$ of HH90 (Φ_L) exceeds it and W05 increases to have a similar value until 02:00 UT. The values from the SuperDARN-based models are again a lot smaller with maximum values of $|\bar{EF}|$ between $\sim$23 and $\sim$31 mV/m. Again TS18 saturates at $\sim$ 20:50 UT whilst TiVIE and Map Potential gradually increase through the main phase.

Panel H is a simple proxy for the convection reversal boundary co-latitude which is approximated by assuming the location of the maximum and minimum potentials lie on a circle containing the polar cap (equation 11). Again the TS18 model saturates at moderate IMF conditions with a convection reversal boundary co-latitude of $\sim 16°$. HH90 and W05 show expansion on similar scales to TiVIE and Map Potential throughout the main phase, despite having a much larger Φ_{PC}. HH90 briefly contracts between 00:35-00:51 UT following the increase of B_z from $\sim -28 \, \text{nT}$ to $\sim -15 \, \text{nT}$. The Map Potential convection map has a smaller radius than the other models during the initial phase of the storm of $9.5°$, before expanding to have the maximum radius of $26°$ at 00:40, 8th. The other models have average convection reversal boundary co-latitudes located between $18°$ and $22°$.

In panel I we show the LLB for the SuperDARN-based models and W05 which we have chosen to be at the midnight boundary. An estimation of the HH90 LLB is included as described in section 2.4. Here the models behave very differently. From 20:00-23:00 UT on the 7th, the W05, TS18 and HH90 (Φ_L) have a similar LLB, stabilising at $\sim 50°$. Shortly after 23:00 UT IMF B_z drops further causing W05, HH90 (Φ_L) and Map Potential to lower their boundaries to $\sim 40°$. TiVIE has a HMB of $\sim 60°$ during the initial phase which drops down to $50°$ during the main phase and does not increase significantly during the first 130 minutes of the recovery phase. The TS18 HMB remains constant at $51.5°$ from 20:50 UT on the 7th to 02:00 UT on the 8th. Map potential and TiVIE, the two models that are not defined using IMF and solar wind parameters (unless there are few SuperDARN vectors available for Map Potential), extend to lower latitudes much later than the other models. Both extend to $\sim 50°$ latitude for the start of the main phase whereas the TS18, HH90 and W05 models extend to $\sim 50°$ latitude at $\sim 21:00$ UT.

3.2 Model comparison of snapshots of convection pattern

Figure 3 shows four snapshots of the convection from each of the models, from left to right: W05, HH90 (Φ_L) (taking Φ_L as the Φ_{PC} input), HH90 (Φ_{Kp}), TS18, Map Potential and TiVIE. From top to bottom the snapshots span 20:00 UT on 7th September

to 02:00 UT on 8th September, in two hour intervals. The snapshot times line up with vertical blue lines from the time series shown in figure 2 and are chosen to show a range of conditions through the initial, main and recovery phases of the storm. The individual plots show northern hemisphere convection maps in AACGM-v2 coordinates with contour lines drawn at 10 kV intervals. Purple/pink represents negative electric potential and blue represents positive electric potential, as shown in the colour bar. A selection of metadata including the time, IMF conditions (B_Y and B_Z), SW velocity, V, Kp, Sym-H and the number of SuperDARN vectors (#SD vecs) are presented above each row.
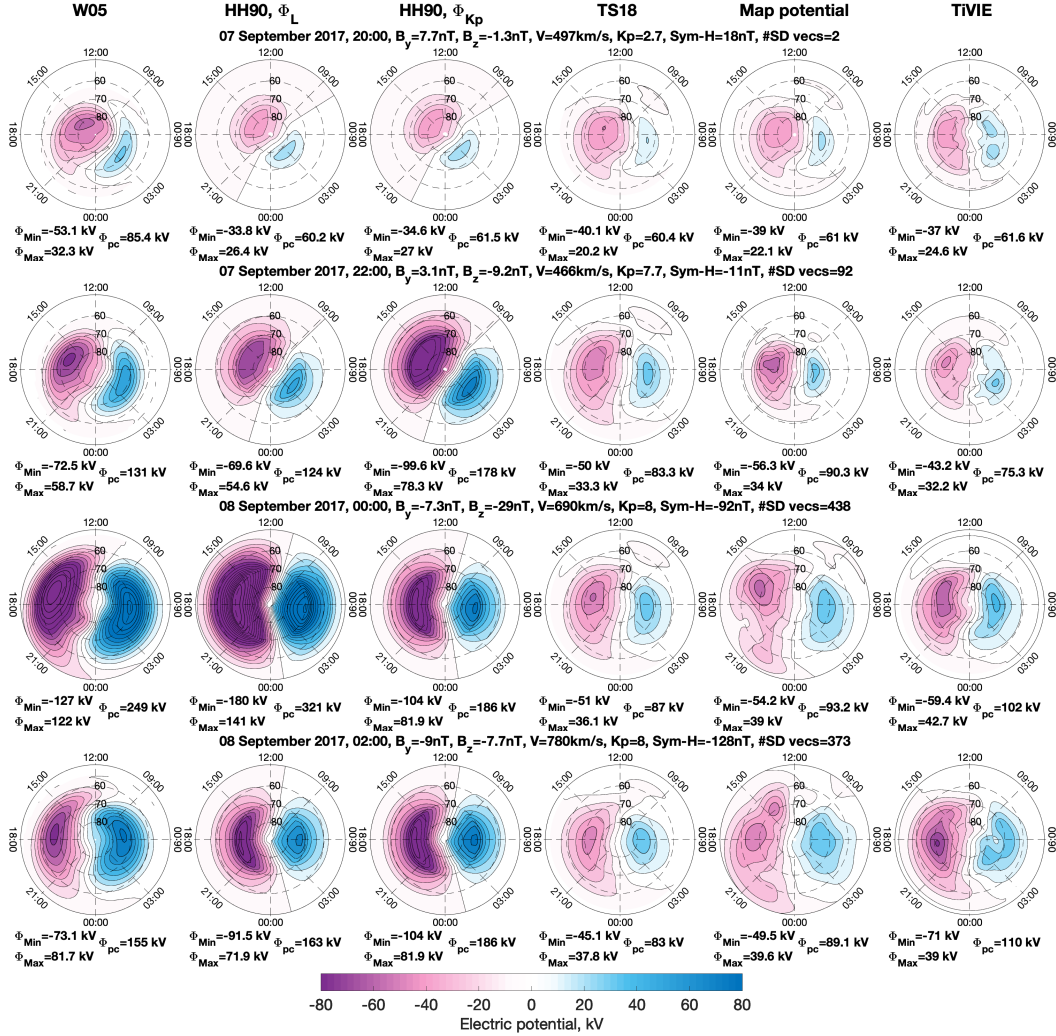
Figure 3. Convection maps in magnetic coordinates with contour lines representing 10kV intervals for the models over four time intervals. Purple/pink represents negative electric potential and blue represents positive electric potential, as shown in the colour bar. A selection of parameters including the time, IMF conditions, SW velocity, Kp, Sym-H and the number of SuperDARN vectors are provided per panel. Text below each map shows the maximum and minimum potential on the left and Φ_{PC} on the right

The first snapshot is during the initial phase when $B_y = 7.7$ nT and $B_z = -1.3$ nT. The convection map produced by W05 descends to $\sim 58°$ latitude in the nightside (around

midnight) and has a maximum and minimum electric potential at 3 and 15 hours MLT respectively. The dusk cell (pink) is centered around 80° latitude, enveloping the magnetic pole, whilst the dawn cell is lower in latitude centered around 70°. The two versions of HH90 give similar patterns with low magnitude electric potential with the convection patterns confined to above $\sim 67°$ latitude on the nightside. Due to the relatively high positive B_y the zero potential lines are rotated 2 hours clockwise of the midnight line and 4 hours clockwise of the noon line. The TS18 convection pattern has a similar shape to W05 but TS18 has $\sim 70\%$ the magnitude of Φ_{PC} from W05. The convection pattern appears to be rotated ~ 3 hours anti-clockwise compared to W05. The Map Potential model in this instance has only 2 SuperDARN vectors available and so is almost exclusively determined by the TS18 model. TiVIE, parameterised only by storm phase, shows a convection pattern for late in the initial phase. The convection pattern resembles TS18/Map Potential patterns with cells roughly symmetrical about the dawn-dusk meridian.

By 22:00 UT the W05 pattern has expanded to lower latitudes, rotated anti-clockwise and Φ_{PC} has increased to 131 kV. HH90 (Φ_L) has maximum and minimum potentials with similar locations and magnitudes to W05, but the location of the dayside and nightside 'throats' is different; note that HH90 defines the zero potential line at ~ 9 and ~ 23 hours MLT owing to the way the model is parameterised. The locations of these zero potential lines are dependent on B_y and do not allow the positive and negative cells to occupy the same local time, in contrast to W05 in the midnight local time sector. HH90 (Φ_{Kp}) has a higher magnitude Φ_{PC} and as such the convection expands equatorward by a further $\sim 2°$ compared to that with the Φ_L input. TS18 is a similar shape to W05 but with much lower Φ_{PC} of 83.3 kV. Compared to HH90 it is rotated anti-clockwise by several hours, and the nightside throat is rotated anti-clockwise by $\sim$1-2 hours compared to W05. Map Potential now has 92 vectors contributing to the fit and so shows a different picture to TS18 and is constrained to higher latitudes. TiVIE resembles TS18 with less uniformity and less asymmetry between the dawn and dusk cells.

By 00:00 UT B_z has reached -29 nT with a SW velocity of 690 km/s, which results in very high electric potential magnitudes. W05 has expanded such that the lower latitude boundary is now located below 50° latitude. The polar cap boundary as inferred from the latitude of the cell foci has expanded in comparison to the map at 20:00 UT. HH90 (Φ_L) has an even higher Φ_{PC} and greater asymmetry between the maximum and minimum potentials. Negative IMF B_y results in an anti-clockwise rotation of $\sim$2 hours of MLT compared to the previous time interval. HH90 (Φ_{Kp}) has the same input Φ_{PC} as at the previous time point, resulting in a similar convection pattern with any differences attributed to the rotation of the convection pattern by 2 hours of MLT due to the decrease of B_y. TS18 has not changed significantly from 22:00 UT because the model has reached its maximum E_{sw} bin. Map Potential extends to lower latitudes and has slightly higher potentials than TS18 but much lower potentials than the W05 and HH90 patterns. TiVIE is now in the main phase of the storm and reaches a higher Φ_{PC} than the other SuperDARN models but still much lower than the W05 and HH90 models.

The main phase of the storm ends at 01:08 UT, and so the final snapshot at 02:00 UT is during the recovery phase of the storm. W05 relies on delayed values of IMF and SW conditions and therefore shows a contracted polar cap with a much lower Φ_{PC} than the previous snapshot. W05 at 02:00 UT is the only map from our chosen snapshots that has a higher magnitude dawn cell than dusk cell as $|\Phi_{max}|$ is higher than $|\Phi_{min}|$. HH90 (Φ_L) likewise uses IMF and SW values so has contracted to higher latitudes. HH90 (Φ_{Kp}) has increased very slightly in magnitude due to Kp increasing from 7.7 to 8. Otherwise the pattern remains the same as above with a further anti-clockwise rotation due to a further decrease in B_y. TS18 is still much the same, as the climatology still corresponds to its highest E_{sw} bin. Map Potential, using SuperDARN measurements from the interval, shows the convection map still extends to lower latitudes (below 50° latitude) and
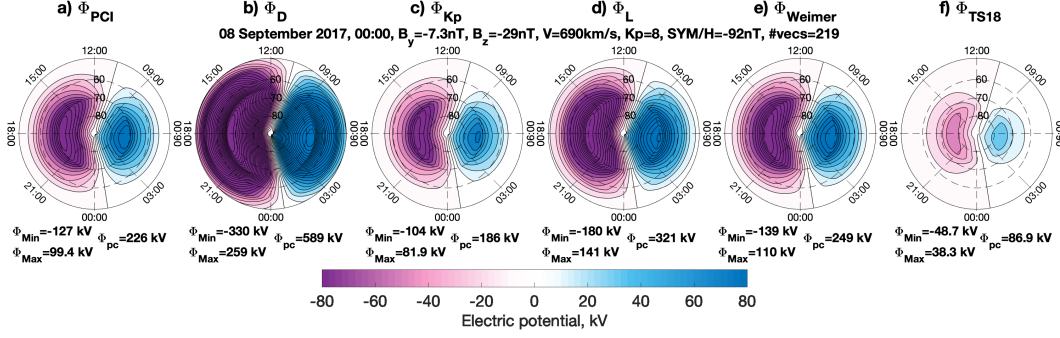
Figure 4. Convection maps in magnetic coordinates with contour lines representing 10 kV intervals for the Heelis model with six Φ_{PC} proxies are four time intervals. Purple/pink represents negative electric potential and blue positive, as shown in the colour bar. A selection of parameters including the time, IMF conditions, SW velocity, PCI, Sym/H and the number of SuperDARN vectors are provided per panel.

still has a similar Φ_{PC} ($\Phi_{PC} \sim 89.1\,\text{kV}$) than the value during the main phase of the storm. TiVIE is now in the recovery phase and mainly shows an increased magnitude of the dusk cell from $-59.4\,\text{kV}$ to $-71\,\text{kV}$.

Figure 4 highlights how big an effect the choice of the Φ_{PC} proxy has on the convection map output by HH90. We show six examples, all for the same time point of 00:00, 8th September. From a) to f) we take the input of Φ_{PC} to be Φ_{PCI} (equation 4), Φ_D (equation 7), Φ_{Kp} (equation 2), Φ_L (equation 1), followed by the Φ_{PC} output by the W05 and TS18 models at the same time point. The rotation of the pattern remains the same for each as it is a function of B_y which remains the same. However the magnitude of the electric potential and the extent to which the pattern expands is very different. Panel f) takes the input of Φ_{PC} to be that which is output from the TS18 model. As TS18 had saturated by this time point, $\Phi_{pc} = 86.9$ kV is much lower than the other estimates of Φ_{PC} and results in the pattern being confined to above $\sim 62°$ latitude. At the other end of the extremes is panel b) which takes the dayside reconnection rate, Φ_D as input. This results in $\Phi_{pc} = 589$ kV, $6.8\times$ higher than the corresponding value from panel f). The remaining maps range from $\Phi_{PC} = 186$ kV using Φ_{Kp} (c) and a $\Phi_{PC} = 321$ kV using Φ_L (d). The lower boundary of the pattern extends from $\sim 58°$ to $\sim 50°$ with the increase in magnitude from c) to d). As it is the Kp equation in c) that is currently used within AENeAS we will continue to compare Φ_{Kp} input throughout our analysis. We will additionally use Φ_L as input to HH90 as a comparison because it is the optimum coupling-function according to Lockwood and McWilliams (2021), and it has a less extreme response to the low B_z values seen within the September 2017 storm.

3.3 Electric Field Vectors for MLT bands

In this section we look in more detail at the variation of the north-south electric field component throughout the storm by taking latitudinal slices across the dawn-dusk line (6 to 18 MLT) and the noon-midnight line (12 to 24 MLT). The electric field vectors were calculated from the gradient of the potential using the method specified in section 2.4. We have converted the north-south electric field vector into Cartesian coordinates such that, along the dawn-dusk line, positive electric field is dawn-to-dusk directed (as shown in the left column of figure 5) and along the midnight-noon line positive electric field is midnight-to-noon directed (as shown in the right column of figure 5). By looking at the MLT bands at dawn (MLT=6) to dusk (MLT=18), and noon (MLT=12) to
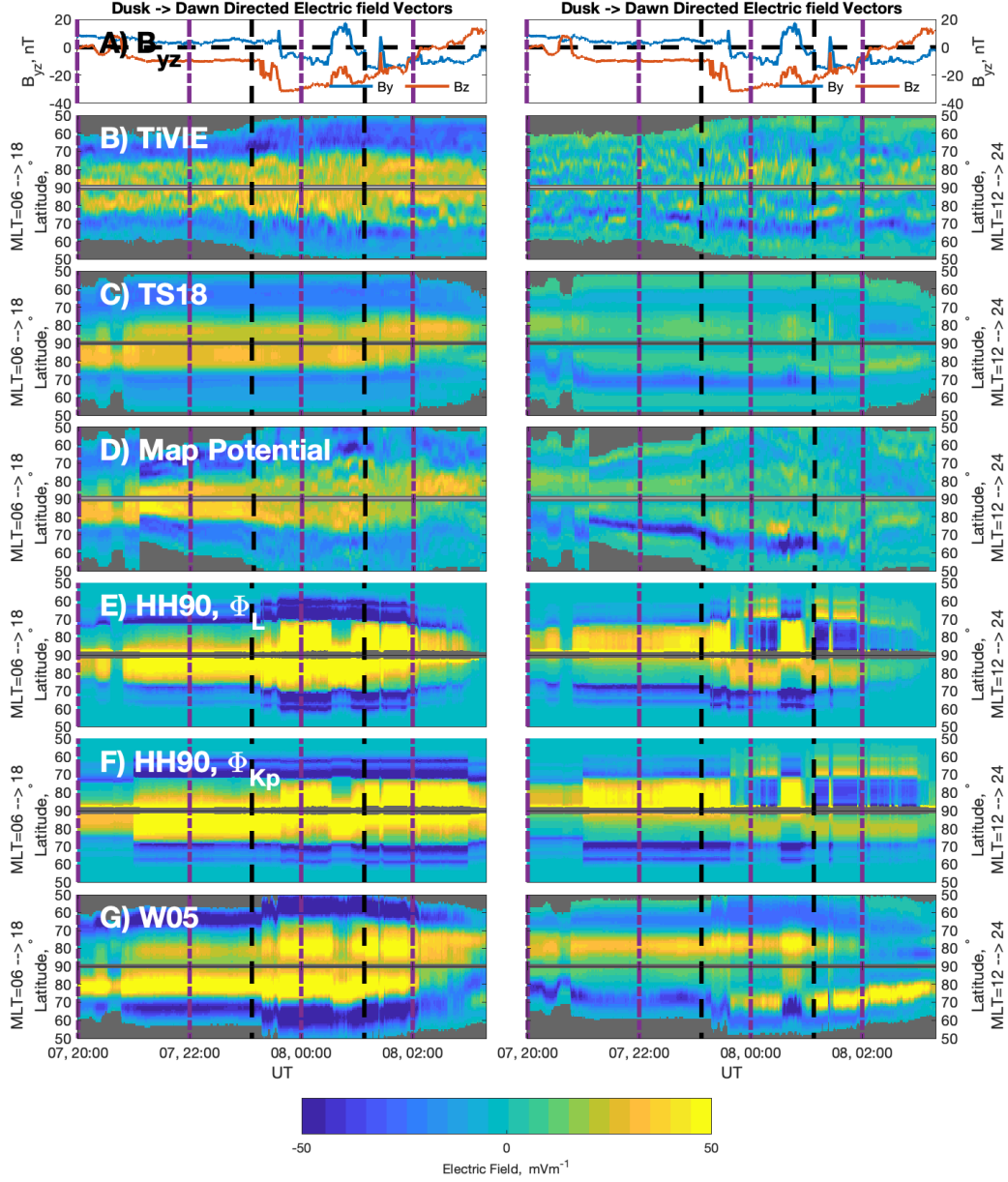
Figure 5. Electric field vectors with left column along the dawn-dusk line with dawn-to-dusk direction and the right column is along the midnight-noon line with midnight-to-noon direction. Panel A has IMF B_y and B_z for reference. Vertical dashed black lines represent the start and end of the main phase. Vertical dashed purple lines match the snapshots from figure 3.

midnight (MLT=24), we see how the topology of the polar cap and lower latitude electric field patterns change throughout the storm, as well as the differences in electric field magnitude between the different models.

In panel A we have plotted the IMF B_y and B_z components of the field for easy comparison with the EF colour plots. The left column plots the dawn-to-dusk directed component of the electric field (EF) according to the colour bar. The x-axis shows the time and the y-axis plots latitude where it increases from $50 - 90°$ latitude along the

MLT=6 line, where it crosses the pole and decreases from $90-50°$ along the MLT=18 line. The right column plots the midnight-to-noon directed component of the EF along the MLT=12 to MLT=24 line. The models are each plotted as rows with B) TiVIE, C) TS18, D) Map Potential, E) HH90 (Φ_L), F) HH90 (Φ_{Kp}) and G) W05 from top to bottom. Colours represent the electric field strength and direction as shown by the colour bar. Grey shows where there is no data, either because it is below the LLB, or it is close to the magnetic pole.

Beginning with the left hand column, we see a dawn-to-dusk directed electric field (positive) within the polar cap (corresponding to anti-sunward flow) and a dusk-to-dawn directed electric field (negative) at auroral latitudes (corresponding to sunward flow). This pattern is consistent across the entire storm with equatorward expansion of the polar cap and the lower latitude boundary evident throughout the storm. Panels E-G, i.e. HH90 (Φ_L), HH90 (Φ_{Kp}), and W05, have higher EF vector magnitudes than the SuperDARN-based models in panels B-D, throughout the storm. TiVIE (Panel B) shows significant variation, particularly in its dawn-to-dusk directed electric field within the polar cap and shows more fine structure compared to the other models. TS18 (Panel C) saturates at $\sim$20:50 UT, as previously seen, and shows a similar pattern from then until 02:00 UT. Map potential (Panel D) shows a sharp change at $\sim$21:06 UT when the model switches from relying heavily on the TS18 climatologies to using available SuperDARN data. Map Potential initially has a relatively strong EF magnitude, both within the pole and at auroral latitudes, but this weakens during the main phase of the storm as the pattern extends to lower latitudes. At auroral latitudes HH90, with both Φ_L and Φ_{Kp} (Panels E-F) has a two-band structure for the dusk-to-dawn directed vectors, with one band centred at around $\sim 70°$ and a thinner band at $\sim 60°$ throughout. HH90 has exponentially decreasing potential outside of the polar cap so no LLB (low latitude grey zone) is shown; the EF magnitude tends towards zero. For all models the overall pattern is reflected across the pole but there are some asymmetries between dusk and dawn. Each of the models has stronger dawn-to-dusk directed EF within the polar cap on the dawn side compared to the dusk side during the initial phase. For TiVIE, TS18, Map Potential and W05 (Panels B-D and G) this pattern continues throughout the main phase of the storm but the HH90 models (Panels E-F) flip to having stronger dusk side EF magnitude within the polar cap when IMF B_y is sufficiently negative e.g. at $\sim$ 23:38-00:32 UT and $\sim$ 00:56-03:18 UT corresponding to when the IMF B_y component switches from positive to negative. W05 shows enhancements in the dusk-side dawn-to-dusk directed field at the same times. TiVIE (Panel B) shows an enhancing dusk-to-dawn directed region of EF (dark blue) shortly after the 22:00 UT in the dusk-side auroral zone.

The right hand column is along the MLT=12 to 24 line, we generally see a midnight-to-noon directed electric field (positive) within the polar cap and a noon-to-midnight directed electric field (negative) at auroral latitudes but the patterns are less consistent than they were along the dawn-dusk line. TiVIE (Panel B) shows more variability with instances of positive and negative vectors scattered around a consistent noon-to-midnight directed strip (blue) of electric field between 65-75° latitude at noon. TS18 (Panel C) shows weak electric field magnitude, particularly below 65°, with the strongest EF being noon-to-midnight directed at auroral latitudes on the noon-side. Likewise Map Potential (Panel D) has relatively weak EF vector magnitude with the strongest vectors being noon-to-midnight directed on the noon-side from $\sim 21:00$ UT, which then expands from $\sim$ 80 degree latitude to $\sim 60°$ by $\sim$ 00:30 UT on the 8th. The noon-side HH90 models, with both Φ_L and Φ_{Kp} (Panels E-F) show a weaker but similar pattern to MLT=18. However at midnight HH90 very clearly shows where the zero potential line is switching from pre to post midnight due to changes in IMF B_y. If $B_y = 0$ the zero potential line is located at 23.5 hours MLT, with negative B_y rotating it clockwise, and positive B_y rotating it anti-clockwise, by 0.15 hours per nT. When $B_y = 0.3$ nT the direction of the electric field bands switch. A plot showing this can be seen in SI, figure S5. W05 (Panel G) has a midnight-to-noon directed EF near the polar cap on the night-

side but only very weak EF within the pole on the dayside throughout, except for during the period of positive B_y around $\sim 00{:}30\,\text{UT}$ when it strengthens. When IMF B_z drops to less than -30 nT at $\sim 23{:}30\,\text{UT}$ there is a strong midnight-to-noon directed EF around 70° latitude at noon, forming a clockwise spiral of equatorward-directed EF from the high latitude negative EF at MLT=18, through noon at 70°, through MLT=6 around 60° and to midnight. This spiral is briefly interrupted at $MLT = 12$ around $\sim 00{:}30\,\text{UT}$ by the switch to positive B_y but reappears around 01:00 UT when B_y returns to negative. See figures S2-3, SI for an example of the global EF for snapshots at the times of the vertical dashed purple lines.

3.4 Direct comparison of models
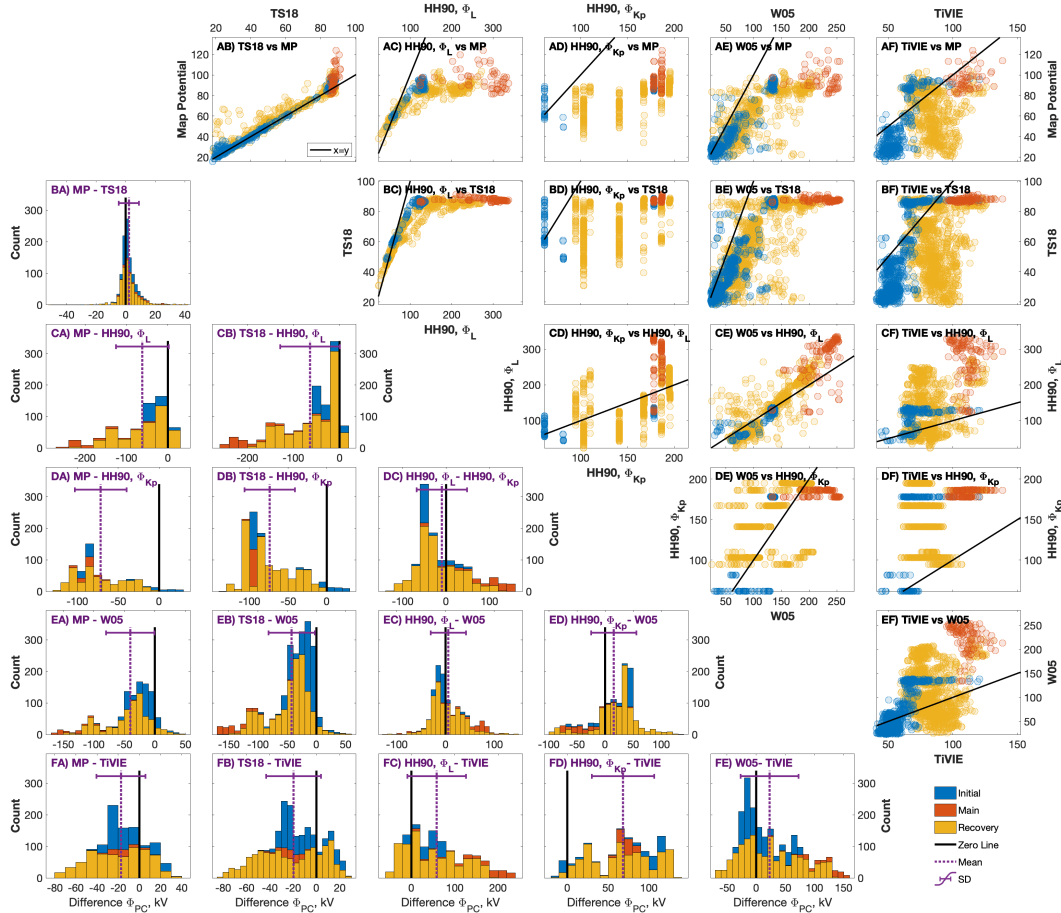
Figure 6. Right side: scatter plots of Φ_{PC}, kV from model A against that of model B at time t. x=y line is in black. Left side: Histogram of Φ_{PC}, kV from model A minus that of model B at time t. The colours represent the phase of the storm at time t. The histograms are are stacked such that the top (blue) represents the initial phase, the middle (orange) the main phase and the bottom (yellow) the recovery phase. The zero difference line is in black, the mean in dashed purple with the standard deviation represented by a horizontal error bar.

In Figures 6 and 7 we show a direct comparison of parameters from 11:02 UT, 7th September until 23:59 UT, 8th September. This is a much wider time range than considered up until now that encompasses all of the initial and main phases of the storm and the first third of the recovery phase (23 of 66 hours). For figure 6 the upper half of

the matrix has scatter plots plotting the transpolar voltage, Φ_{PC}, from model A against that of model B at time t. The $x = y$ line is included to show where the points would lay if the model output was the same. If the points are above the $x = y$ line the model on the y-axis has a larger Φ_{PC} than the model on the x-axis at that time. For figures 6 and 7 the times included are from 11:02 UT, 7th September, the start of the initial phase, until 23:59 UT, 8th September, during the recovery phase.

On the bottom half of the matrix we show histograms of Φ_{PC} from model A minus Φ_{PC} from model B. The black line marks zero difference and is equivalent to x=y, i.e., if the two models were the same the distribution would be a delta function at zero. The mean difference in the models Φ_{PC} is overplotted with a dashed purple line with the standard deviation represented as a horizontal error bar about the mean.

The panels are organised as a grid such that the first row is map potential on the y-axis vs each of the models on the x-axis in each column. The first column shows the histograms of map potential minus each of the models. Each row is labelled by the first model (A-F) and each column is labelled by the second model (A-F) such that AB) is the scatter plot of TS18 vs Map Potential (MP) and the corresponding histogram BA) is Map Potential minus TS18. The colours represent the phase of the storm. The histograms are are stacked vertically such that the top (blue) represents the initial phase, the middle (orange) the main phase and the bottom (yellow) the recovery phase. The histograms are not overlapping i.e. the main phase has the lowest counts as it contains the fewest time points.

Panel AB) shows that there is a clear saturation in TS18 at ∼90 kV, with the main phase of the storm varying from $\sim 80-120$ kV for Map potential but Φ_{PC} from TS18 only from $\sim 85-91$ kV. BA) shows TS18 and Map potential are the most similar, with the histogram centred around zero with a slight bias towards Map potential having stronger Φ_{PC} than TS18 (mean difference of 2.3 kV). AC)-AE) show that Map potential saturates compared to HH90 and W05. All models but TS18 tend to have stronger Φ_{PC} than Map Potential for the same time point. This is demonstrated by the points being below the x=y line in row A. Similarly, the histograms of Map potential in column A are biased towards negative values as all models but TS18 have generally higher Φ_{PC}, especially during the main phase, and negative mean differences. In the row B scatter plots TS18 (y-axis) again shows a clear saturation of ∼90 kV throughout. In BC) HH90 (Φ_L) is relatively similar to TS18 until this saturation point. In column B each histogram is shifted towards negative values and has a negative mean difference showing that Φ_{PC} for TS18 is smaller than each of the other models. In CE) HH90 (Φ_L) and W05 show high correlation with Φ_L generally having slightly higher Φ_{PC} than W05. The corresponding histogram EC) is almost centred around zero (mean difference of 5.6 kV) but with a standard deviation of 36 kV. During the main phase Φ_L can be ∼50-80 kV higher than that of W05. Φ_L shows the highest variability compared to the other models with differences between Φ_L and all models but W05 having a standard deviation of $58 - 68$ kV. The scatter plots in column/row D show that the Φ_{Kp} proxy (equation 2) is ordered in discrete steps and it consequently does not have much correlation with the other models. In column F, TiVIE shows a spread in all cases. Towards the end of the initial phase (in blue; $\sim 20:50$ UT to beginning of main phase) TiVIE gradually increases from $\sim 60-120$ kV whilst each of the other models remains constant (as was seen in figure 2).

Figure 7 is of the same form as figure 6 but shows a comparison of the LLB/ HMB for the models. As for figure 2, the LLB is the HMB for the SuperDARN-based models and the LLB at the midnight boundary for W05. An estimation of the HH90 LLB is included as described in section 2.4. The convection maps from all but the HH90 models are calculated at 1° discrete steps and hence a randomised value between ±0.5° is added to the LLB to aid the visualisation of the density of discrete data. Without this the discrete points are likely to be overplotted, making it difficult to distinguish between
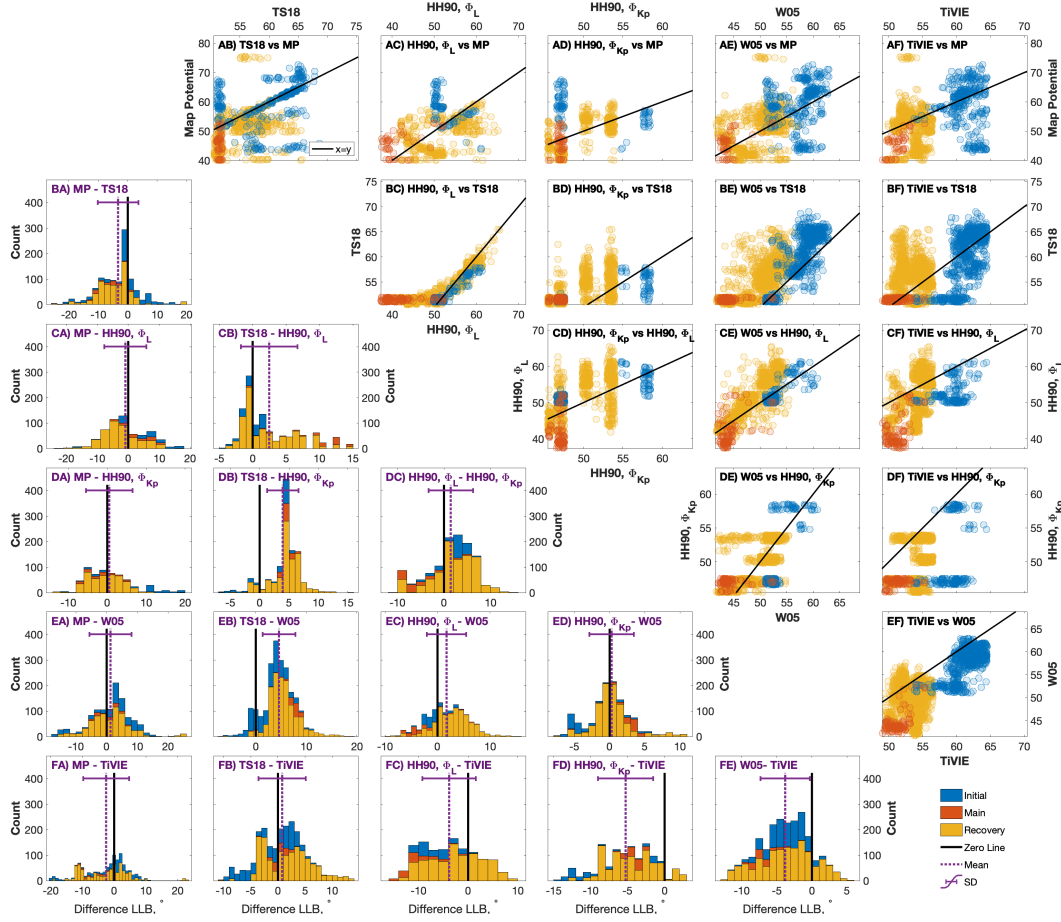
Figure 7. Right side: scatter plots of the lower latitude boundary from model A against that of model B at time t. x=y line is in black. Left side: Histogram of lower latitude boundary from model A minus that of model B at time t. The colours represent the phase of the storm at time t. The histograms are are stacked such that the top (blue) represents the initial phase, the middle (orange) the main phase and the bottom (yellow) the recovery phase. The zero difference line is in black, the mean in dashed purple with the standard deviation represented by a horizontal error bar.

low and high density data occurrence. The magnetic latitude of HH90 is calculated as described in section S1.2 of the SI.

In figure 6 we saw high correlation between Φ_{PC} of TS18 and Map Potential. In figure 7 we see little correlation between the LLB of TS18 and Map potential in panel AB). Map potential generally has a lower boundary than TS18 as indicated by most of the points being below the x=y line, and the negative shifted histogram in BA) which has a mean of -3.3°. Column/row A shows Map potential and the other models have little correlation and a lot of scatter. BC) shows high correlation between HH90 (Φ_L) and TS18, until the TS18 LLB saturates at 51 ° (corresponding to the previous saturation seen in electric potential during the main phase of the storm). W05 and TiVIE in columns E and F show the LLB at distinct latitude bands in the initial, main and recovery phases. For TiVIE (column F) the initial phase has a LLB centred around $60-65°$, main $\sim 50°$ and recovery $\sim 52-57°$. For Weimer (column E) the initial phase has a LLB centred between $50-63°$, main $\sim 42-45°$ and recovery $\sim 42-57°$. During the initial phase

676 the TiVIE LLB changes from 50−60° whilst TS18, HH90 (Φ_L), HH90 (Φ_{Kp}), and W05
677 have a constant lower boundary; this is shown by the horizontal line of blue markers in
678 column F. The majority of the histograms are centred around the zero line, with much
679 less shift toward the positive/negative than was seen in figure 6. Standard deviations range
680 between 2.7° in DB) and 7.2° in FA). Exceptions include TS18 compared to HH90 (Φ_{Kp})
681 (DB) and to W05 (EB) which are shifted to the positive i.e., they have a significantly
682 lower LLB than TS18, as well as HH90 (Φ_{Kp}) compared to TiVIE (FD) which has a mean
683 of -5.3°.

4 Discussion

685 The aim of this study was to compare the output of modern high-latitude ionospheric
686 electric field models, based on SuperDARN measurements, to older models based on space-
687 craft data. Electric field models represent an important component of thermospheric mod-
688 els due to their influence on Joule heating (Bruinsma et al., 2021). It is possible that in-
689 corporating the more modern models into large atmosphere models such as AENeAS will
690 improve their forecasting ability. We have compared the versions of the Heelis model (HH90)
691 (Heelis et al., 1982; M. Hairston & Heelis, 1990; HAO, 2018), and the Weimer model (W05)
692 (Weimer, 2005) that are both implemented in AENeAS with the Thomas and Shepherd
693 (TS18) (Thomas & Shepherd, 2018) and TiVIE mode 3 models (Walach & Grocott, 2022),
694 as well as the SuperDARN Map Potential (Ruohoniemi & Baker, 1998), during the Septem-
695 ber 2017 geomagnetic storm. During geomagnetic storms, Joule heating is significantly
696 enhanced. Hence, it is important to be able to forecast well for storm time conditions.
697 In this section we highlight the differences in the electric field contribution to Joule heat-
698 ing that arise from the different models during storm times and the possible reasons for
699 the differences.

700 Although we are only studying a single storm it encompasses a wide range of so-
701 lar wind and IMF conditions to highlight differences in both the model topologies and
702 magnitudes. The W05, HH90 (Φ_L) and TS18 models are calculated using 1-min cadence
703 solar wind and IMF data as input, and as such are directly sensitive to the variability
704 in these parameters. HH90 (Φ_{Kp}) is dependent on the 3-hourly Kp index as well as 1-
705 minute cadence IMF B_y. TiVIE is parameterised by storm phase and so is not directly
706 sensitive to variations in the solar wind drivers but is designed to better capture the time
707 history of the magnetospheric response. As a forecast model, however, TiVIE is limited
708 by the need to await the start and end of each storm phase. Map Potential uses Super-
709 DARN measurements of the event, so it is not suitable for forecasting either but can act
710 as a baseline, with the caveat that two of the other models we are comparing it to are
711 also based on SuperDARN data.

712 The variations in the magnitudes of the electric potential outputs across the ob-
713 served range of conditions highlight some of the main differences between the models.
714 Under quiet and moderate conditions the models display relatively similar outputs. This
715 is particularly clear during the initial and recovery phases in figure 6. Hence, we would
716 expect estimates of Joule heating to be relatively consistent between models at these times.
717 However, when IMF B_z drops towards −30 nT, the spacecraft-based models (W05 and
718 HH90) can have more than double the transpolar voltage of the SuperDARN-based mod-
719 els. This would relate to a difference in Joule heating estimates of more than a factor
720 of 4.

721 For the TS18 model the primary reason for the underestimation with respect to
722 the spacecraft-based models is simple. When $B_z < -10$ nT in Figure 2, Φ_{PC}, r_{pc}, and
723 HMB in TS18 all saturate at ∼90 kV, 15°, and 51°, respectively. This is because $E_{sw} >$
724 3 mV/m, $110 < \theta_{clk} < 250°$, and dipole tilt is neutral during this time. In this range,
725 there are only three potential patterns available in the TS18 model which all have quite
726 similar r_{pc} and HMB and Φ_{PC} only varies between 84 and 91 kV (see figure 6 and Ta-

ble 2 of TS18). The data used in TS18 was collected during solar cycle 24, which was a much less active solar cycle than solar cycle 21, when the data used in W05 was collected (see figure 1). Thomas and Shepherd (2018) lowered their solar wind electric field magnitude, E_{sw} bins to account for the smaller measurements compared to previous SuperDARN models (Ruohoniemi & Greenwald, 1996; Pettigrew et al., 2010; Cousins & Shepherd, 2010). This restriction suggests that this model is not wholly suitable for describing variations in convection during extreme storm times. This is unsurprising given the model is designed as a background model for the Map Potential. Thomas and Shepherd (2018) have a Kp counterpart statistical characterisation of ionospheric convection which is parameterised by Kp and IMF clock angle. The highest Kp bin (< 8) shows a $-B_z$ convection pattern that extends to lower latitudes on the nightside and has higher magnitude electric potential than the highest E_{sw} bin ($3.0 \leq E_{SW} < 20.0 \, \text{mV/m}$ (Thomas & Shepherd, 2018). The maximum value of Φ_{PC} using the Kp version of TS18 is $\sim 97 \, \text{kV}$ which is still below the maximum values of Φ_{PC} found using each of the other models during this September 2017 event.

For Map Potential the E_{sw} constraint is partly removed because of the addition of SuperDARN measurements from the September 2017 storm itself. r_{pc} and HMB expand equatorward to latitudes comparable to W05 and HH90 (Φ_L) but Φ_{PC} for Map Potential increases to $< \sim 120 \, \text{kV}$ (30% increase) compared to $> \sim 200 \, \text{kV}$ for W05 and HH90 (Φ_L). This suggests that either the large-scale Φ_{PC} measure is still heavily constrained by the TS18 model and/or other factors are at play. Firstly, SuperDARN has been known to underestimate the Φ_{PC} when the polar cap expands beyond the field of view of the radars (S. Shepherd et al., 2002). Since this study, the SuperDARN network has expanded to both higher and lower latitudes. However, Thomas and Shepherd (2018) acknowledge that during extreme events Φ_{PC} is likely to underestimated due to the convection pattern expanding equatorwards of the mid-latitude radars. This may be the case for the extreme storm time variations considered here as the HMB saturates at 40°, which is an artificial limit in the model due to the lowest available latitude of radar measurement. Secondly, it has also been noted that when compared to DSMP ion drifts, SuperDARN velocities have been shown to be smaller (Drayton et al., 2005). Doppler velocities measured by SuperDARN are progressively under-estimated with decreasing ionospheric refractive index caused by increasing electron density (Gillies et al., 2009), which may be expected due to enhanced auroral particle precipitation during higher Φ_{PC} and corresponding geomagnetic activity.

For TiVIE, although it is not constrained by TS18, it is based on SuperDARN data and so could be underestimating Φ_{PC} during extreme events due to the refractive index and the pattern extending beyond the equatorward extent of the radars; indeed the TiVIE HMB saturates close to 50°, like TS18. Alternatively, or additionally, TiVIE mode 3 is calculated from 54 storms during solar cycle 24, the same time period as TS18, of which only two storms (Sep 26, 2011 and June 22, 2015) have a more negative B_z than that seen in the September 7th-8th, 2017 storm. Likewise, only two (Mar 09, 2012 and June 22, 2015) have Kp higher than or equal to that seen in the Sep 7, 2017 storm, meaning this storm is towards the more extreme end of the events used within TiVIE. This could suggest that TiVIE is biased to underestimate Φ_{PC} during more extreme storms than the average storm of solar cycle 24. However, one feature of TiVIE is that it does provide a forecast of the temporal variability introduced to the convection electric field during a storm by the inclusion of time history. The delayed solar wind values used as input for W05, HH90 and TS18 may result in over or under estimations of the magnitude of Φ_{PC} as these models take no account of how long the B_z component has been negative, which is an indication of how much energy has been added to the system through reconnection.

In contrast to the TS18 and TiVIE models whose solutions are binned averages that are constrained to the ranges of the data used in their development, there is no such re-

striction in the HH90 and W05 models. By construction, the ionospheric electric potential solution in these models is described by parameters that are continuous functions of the input control variables, allowing the solutions to be extrapolated even beyond the range of the underlying observations. However the choice of parameter functions differs within the HH90 model and between it and the W05 model. For HH90 the strong potentials seen during the main phase of the storm are a result of the input parameter Φ_{PC}; the maximum potential in the dawn cell is always 44% of Φ_{PC} and minimum potential in the dusk cell is always -56% of Φ_{PC}. Maps showing the effect of the choice of Φ_{PC} proxy are included in figure 4, clearly showing how the choice of this input parameter affects the size and magnitude of the convection pattern.

The Φ_{PC} output from the W05 model is most similar to the Lockwood parameter Φ_L, which we used in HH90 but the W05 model does contain a saturation curve that levels to a gradual slope at higher magnitudes of the solar wind electric field (Weimer, 2005) (equation 3 in Weimer (2005)). There have been many observational, theoretical, and modelling studies e.g. (M. R. Hairston et al., 2005; S. G. Shepherd, 2007; Kubota et al., 2017), that have found saturation of Φ_{PC} for large E_{SW}. S. G. Shepherd (2007) suggests Φ_{PC} saturates at $< 300\,\text{kV}$ whilst Lockwood and McWilliams (2021) suggests a typical value between $150-200\,\text{kV}$. Figure S7 plots E_{SW} vs Φ_{PC} which shows the saturation of W05 at ~ 250 kV to be much higher than the artificial saturation of the SuperDARN based models and Φ_{Kp}. Φ_L shows a curved relationship with E_{SW} similar to W05 for lower values but it does not saturate.

The polar cap radius proxy, r_{pc} and the lower latitude boundary (or HMB) variations show both boundaries moving equatorward throughout the main phase of the storm as the Φ_{PC} increases. The HH90 (Φ_L) and HH90 (Φ_{Kp}) polar caps are smaller than or similar in size to many of the other models despite having a considerably higher Φ_{PC}. The equation HH90 used to define the convection flow reversal circle is $\theta_0 = -3.8° + 8.48°\Phi_{pc}^{0.1875}$, similar to equations found in G. L. Siscoe (1982) and M. Hairston and Heelis (1990). Although this is not the same as the polar cap radius proxy we have chosen to represent the size of the polar cap (equation 11), it provides an estimate of how big the defined HH90 radius can be (see figure S6 in SI). No other model is restricted by this equation; they can have larger polar cap radii per Φ_{PC} than HH90. The expanding-contracting polar cap (ECPC) paradigm (G. Siscoe & Huang, 1985; Lockwood & Cowley, 1992; Milan et al., 2007) defines the rate of change of open flux in the polar ionosphere as the difference between dayside and nightside reconnection rates. Open flux increases when dayside reconnection exceeds nightside reconnection and decreases when nightside reconnection exceeds dayside reconnection. While the dayside reconnection rate is directly related to interplanetary conditions, the nightside rate is only weakly related to the IMF; it is dependent on the magnetic shear across the magnetotail current sheet (Lockwood et al., 2009). Therefore whilst it is likely that a large Φ_{PC} will be associated with an increased polar cap size, it cannot be directly attributable. A large Φ_{PC} driven equally by dayside and nightside reconnection would not impact the size of the polar cap, and a large Φ_{PC} driven predominantly by nightside reconnection would cause the size of the polar cap to shrink.

As with the polar cap boundary variation, the LLBs are also highly variable. HH90 does not have a strict LLB as it is an exponentially decreasing function equatorward of the convection reversal boundary. However, we define a potential magnitude that provides an estimate of where the boundary would be (equivalent to the W05 mean potential at the midnight HMB). Figure 3 and figure 5 show that the HH90 convection does not extend to as low a latitude as many of the other models. HH90 does not have $|EF| > 25$ mV/m in the north-south component below 60° magnetic latitude at dawn or dusk, or at midnight or noon at any point during our time interval; all other models extend equatorward of this. However in figure 2, HH90 (Φ_L) has a lower boundary similar to W05 and Map Potential through the main phase of the storm. Figure 7 shows the bound-

ary from HH90 (Φ_L) to be lower than each of the other models during the main phase. In terms of the HMB, TiVIE has similar limits to TS18, despite its saturation. W05 and Map Potential extend $\sim 10°$ lower than TiVIE and TS18 during the main phase. Part of this may be due to the issues with poor HMB placement using the current algorithm within Map Potential (Fogg et al., 2020).

The fixed HH90 shape is also worth mentioning. The zero potential lines at midnight and noon are defined solely by the value of IMF B_y. The convection cells cannot overlap in MLT so this line is critical to the shape and longitudinal spread of the dawn and dusk cells. AENeAS hard codes limits of $-11 \leq B_y \leq 7$ nT to restrict the placement of the zero potential line in the northern hemisphere to stop the pattern rotating excessively and the potential at the centre of the pattern having a higher potential than the maximum and minimum values seen at the centre of the convection cells. However, this presents further problems with these defined boundaries during times of strong IMF B_y. It is clear from the snapshots in figure 3 that large changes in B_y have a significant effect on the rotation of the HH90 convection pattern, a rotation that is not obvious in the other models. In terms of the north-south component of the electric field, small changes in IMF B_y result in sign changes in the electric field measured at noon and midnight. This effect is highlighted in SI figure S5. Figure 5 further highlights the problems with the fixed boundary at 24:00 MLT. The electric field switches from strongly positive to strongly negative, and vice-versa, due to longitudinal changes in the location of the zero potential line that are purely a function of B_y variability. If $B_y = 0$, the zero potential line enters at 23.5 hours MLT, with negative B_y rotating it clockwise, and positive B_y rotating it anti-clockwise, by 0.15 hours per nT. When $B_y < 0.3$ nT the direction of the electric field bands switch.

The differences in both the size of the polar cap and the latitude of the LLB between the different models are important as they will have knock on effects in atmospheric models like AENeAS. For example, if a model places the LLB at too high a latitude then a region will be predicted to have zero electric field instead of a non-zero electric field and this will impact Joule heating estimates. The effects on Joule heating are less straightforward in terms of the radius of convection reversal (for which we use the polar cap radius proxy, r_{pc}) but it is possible to envisage a situation where, if r_{pc} is changing, the electric field direction is likely to be switching (as the boundary moves above and below a given geographical region). We know from Deng et al. (2009) that electric field variability (and not just magnitude) is key to Joule heating.

5 Conclusions

Models of the high-latitude ionospheric electric field are commonly used to specify the magnetospheric forcing in modern atmosphere models. The use of decades-old spacecraft-based models is still widespread. However, modern radar-derived electric field models could improve forecasting functionally. We have compared the AENeAS version of the Heelis model (Heelis et al., 1982; M. Hairston & Heelis, 1990; HAO, 2018) referred to as HH90, the Weimer model (W05) (Weimer, 2005), Thomas and Shepherd (TS18) (Thomas & Shepherd, 2018) and TiVIE (Walach & Grocott, 2022), as well as the SuperDARN Map Potential. Here we compare the electric field models during the September 2017 storm, covering a range of solar wind and IMF conditions. We explore the relationships between the IMF conditions and model output parameters and find:

- TS18 consistently has the lowest electric potential output and does not expand to low latitudes during the September 2017 storm. This is primarily because the TS18 model was developed using data from the relatively benign solar cycle 24 and has only one ionospheric electric potential solution for a solar wind electric field value $E_{sw} > 3$ mV/m (for given IMF B_y and dipole tilt). Thus TS18 is not suitable for use in AENeAS during storm times. If this model could be extended

884 using a much larger SuperDARN data set over multiple solar cycles then it might
885 be possible to produce a more accurate model version.
886 • TIVIE mode 3 is parameterised by storm phase timings, not IMF and SW con-
887 ditions. Its output therefore misses details associated with the individual storm.
888 This variability could be captured by introducing additional parameterisation to
889 TiVIE. Like TS18, TiVIE was developed using data from solar cycle 24 and thus
890 is biased to ionospheric electric potential solutions appropriate to weaker storms.
891 • HH90 is hugely dependent on the Φ_{PC} proxy used as input. HH90 based on Kp
892 (as used in AENeAS) has very poor temporal resolution which makes it unsuit-
893 able form many applications. To use HH90 requires a potential proxy that has been
894 well tested in storm conditions.
895 • HH90 (Φ_L) is comparable to Weimer in electric potential magnitude and convec-
896 tion pattern topology but the transpolar voltage differs by $\sim$50% during peak storm
897 times.

898 Based on these findings we conclude that the main difference between models is
899 that the parameters of the spacecraft-based electric potential solutions are fit to a con-
900 tinuous function of the input control variables, whereas the SuperDARN-based solutions
901 are averages for comparable observed input conditions (e.g., binned by E_{sw}, or time within
902 the storm). Consequently, the spacecraft-based models are designed to extrapolate to
903 extreme conditions even beyond those observed whereas the SuperDARN-based mod-
904 els are constrained to the conditions available within the data used to develop them. This
905 causes the SuperDARN-based model metrics to reach an artificial limit for rare extreme
906 conditions, such as the apparent saturation of the transpolar voltage at $\sim$100 kV. This
907 is also exacerbated by the known systematic under-estimation of the ionospheric elec-
908 tric field by high frequency radars due to the ionospheric refractive index being less than
909 the assumption of unity and limits introduced by the low latitude extent of the Super-
910 DARN radars. However, whilst the spacecraft-based models have no such limits, their
911 solutions have high uncertainty because they are based on limited data or are extrap-
912 olations beyond the observed range based on equations with different functional forms.

913 Consequently, we recommend that efforts to nowcast and forecast the thermosphere
914 using ensemble models such as AENeAS include an analysis of the effects of the uncer-
915 tainties in the underlying electric field models. This could be achieved by comparing the
916 degree of satellite drag predicted using such models to direct satellite drag observations.
917 In addition, more work should be done in further developing ionospheric electric field mod-
918 els during geomagnetic storms, especially by including more data from periods of high
919 geomagnetic activity. A greater understanding of the relevant physics such as transpo-
920 lar voltage saturation and the refractive index effect are needed to bring the model pre-
921 dictions closer together.

6 Open Research

923 The version of the Heelis model used for the analysis in this paper is taken from
924 TIEGCM (Qian et al., 2014), a model within AENeAS (Elvidge & Angling, 2019; HAO,
925 2018). A full description of the code is included in the SI. A full version of TIEGCM code
926 can be downloaded from `https://www.hao.ucar.edu/modeling/tgcm/download.php`.
927 The W05 code was provided by D. Weimer. It is available as an IDL model (Weimer,
928 2019), but the version used in this paper is the Fortran 90 code used within TIEGCM
929 and is available as part of the aforementioned download. TS18 is available using the 'solve_model'
930 module as part of the Radar Software Toolkit (RST Version 4.6) (SuperDARN Data Anal-
931 ysis Working Group et al., 2021), available for download at `https://superdarn.github`
932 `.io/dawg/software/`. Map Potential and TiVIE were processed using the 'maptoefield'
933 RST module to find the electric potential from the fit.map files. The Map Potential data
934 processing is described fully in (Walach et al., 2022) and we use the equivalent of their

'D4' dataset. This includes data from all the northern hemisphere radars, which were processed using a range gate limit from 800-2000km and the TS18 background model. Where there are data gaps, model vectors are infilled from the TS18 background model. TiVIE storm mode phases are available from the Lancaster University's research archive (PURE), Ionospheric Electric Field Morphologies during Geomagnetic Storm Phases 2.0, `https://doi.org/10.17635/lancaster/researchdata/417`. Heppner-Maynard-Rich Electric Field Model 1990 available from `https://git.smce.nasa.gov/ccmc-share/ modelwebarchive/-/tree/main/Heppner-Maynard-Rich_Electric-Field-Model`. Sunspot data is from `https://www.sidc.be/silso/infosnmtot` (downloaded 14th October 2021). NASA OMNI data is available at `http://omniweb.gsfc.nasa.gov/ow.html` (downloaded 19th January 2021). Conversion from magnetic coordinates to geographic is calculated using the AACGM-v2 library (S. Shepherd, 2014; Burrell et al., 2020). The SuperDARN data are available from the BAS SuperDARN data mirror `https://www.bas.ac.uk/project/ superdarn`.

References

Boyle, C., Reiff, P., & Hairston, M. (1997). Empirical polar cap potentials. *Journal of Geophysical Research: Space Physics*, *102*(A1), 111–125.

Bristow, W. A., Topliff, C., & Cohen, M. B. (2022). Development of a high-latitude convection model by application of machine learning to superdarn observations. *Space Weather*, *20*(1), e2021SW002920.

Bruinsma, S., Boniface, C., Sutton, E. K., & Fedrizzi, M. (2021). Thermosphere modeling capabilities assessment: geomagnetic storms. *Journal of Space Weather and Space Climate*, *11*, 12.

Burrell, A., van der Meeren, C., & Laundal, K. M. (2020, January). *aburrell/aacgmv2: Version 2.6.0.* Zenodo. Retrieved from `https://doi.org/ 10.5281/zenodo.3598705` doi: 10.5281/zenodo.3598705

Chisham, G., Lester, M., Milan, S. E., Freeman, M. P., Bristow, W. A., Grocott, A., ... Walker, A. D. M. (2007). A decade of the Super Dual Auroral Radar Network (SuperDARN): scientific achievements, new techniques and future directions. *Surveys in Geophysics*, *28*, 33-109.

Cousins, E., & Shepherd, S. (2010). A dynamical model of high-latitude convection derived from superdarn plasma drift measurements. *Journal of Geophysical Research: Space Physics*, *115*(A12).

Deng, Y., Maute, A., Richmond, A. D., & Roble, R. G. (2009). Impact of electric field variability on joule heating and thermospheric temperature and density. *Geophysical Research Letters*, *36*(8).

Dickinson, R. E., Ridley, E., & Roble, R. (1981). A three-dimensional general circulation model of the thermosphere. *Journal of Geophysical Research: Space Physics*, *86*(A3), 1499–1512.

Dimmock, A. P., Rosenqvist, L., Hall, J.-O., Viljanen, A., Yordanova, E., Honkonen, I., ... Sjöberg, E. (2019). The gic and geomagnetic response over fennoscandia to the 7–8 september 2017 geomagnetic storm. *Space Weather*, *17*(7), 989–1010.

Drayton, R., Koustov, A., Hairston, M., & Villain, J.-P. (2005). Comparison of dmsp cross-track ion drifts and superdarn line-of-sight velocities. In *Annales geophysicae* (Vol. 23, pp. 2479–2486).

Elvidge, S., & Angling, M. J. (2019). Using the local ensemble transform kalman filter for upper atmospheric modelling. *Journal of Space Weather and Space Climate*, *9*, A30.

Farris, M., & Russell, C. (1994). Determining the standoff distance of the bow shock: Mach number dependence and use of models. *Journal of Geophysical Research: Space Physics*, *99*(A9), 17681–17689.

Fogg, A., Lester, M., Yeoman, T., Burrell, A., Imber, S., Milan, S., . . . Anderson, B. (2020). An improved estimation of superdarn heppner-maynard boundaries using ampere data. *Journal of Geophysical Research: Space Physics*, *125*(5), e2019JA027218.

Gillies, R., Hussey, G., Sofko, G., McWilliams, K., Fiori, R., Ponomarenko, P., & St.-Maurice, J.-P. (2009). Improvement of superdarn velocity measurements by estimating the index of refraction in the scattering region using interferometry. *Journal of Geophysical Research: Space Physics*, *114*(A7).

Grocott, A., Badman, S. V., Cowley, S., Milan, S. E., Nichols, J. D., & Yeoman, T. K. (2009). Magnetosonic mach number dependence of the efficiency of reconnection between planetary and interplanetary magnetic fields. *Journal of Geophysical Research: Space Physics*, *114*(A7).

Hairston, M., & Heelis, R. (1990). Model of the high-latitude ionospheric convection pattern during southward interplanetary magnetic field using de 2 data. *Journal of Geophysical Research: Space Physics*, *95*(A3), 2333–2343.

Hairston, M. R., Drake, K. A., & Skoug, R. (2005). Saturation of the ionospheric polar cap potential during the october–november 2003 superstorms. *Journal of Geophysical Research: Space Physics*, *110*(A9).

HAO. (2018). *Tiegcm v1.94 model description.* Retrieved from `https://www.hao.ucar.edu/modeling/tgcm/doc/description/model_description.pdf`

Heelis, R., Lowell, J. K., & Spiro, R. W. (1982). A model of the high-latitude ionospheric convection pattern. *Journal of Geophysical Research: Space Physics*, *87*(A8), 6339–6345.

Heppner, J., & Maynard, N. (1987). Empirical high-latitude electric field models. *Journal of Geophysical Research: Space Physics*, *92*(A5), 4467–4489.

Heppner, J. P. (1977). Empirical models of high-latitude electric fields. *Journal of Geophysical Research*, *82*(7), 1115–1125.

Khan, H., & Cowley, S. (1999). Observations of the response time of high-latitude ionospheric convection to variations in the interplanetary magnetic field using eiscat and imp-8 data. In *Annales geophysicae* (Vol. 17, pp. 1306–1335).

Kubota, Y., Nagatsuma, T., Den, M., Tanaka, T., & Fujita, S. (2017). Polar cap potential saturation during the bastille day storm event using global mhd simulation. *Journal of Geophysical Research: Space Physics*, *122*(4), 4398–4409.

Liu, H.-L., Bardeen, C. G., Foster, B. T., Lauritzen, P., Liu, J., Lu, G., . . . others (2018). Development and validation of the whole atmosphere community climate model with thermosphere and ionosphere extension (waccm-x 2.0). *Journal of Advances in Modeling Earth Systems*, *10*(2), 381–402.

Lockwood, M., & Cowley, S. (1992). Ionospheric convection and the substorm cycle. *In: 'Substorms 1, Proceedings of the First International Conference on Substorms, ICS-1'*, 99–109.

Lockwood, M., Hairston, M., Finch, I., & Rouillard, A. (2009). Transpolar voltage and polar cap flux during the substorm cycle and steady convection events. *Journal of Geophysical Research: Space Physics*, *114*(A1).

Lockwood, M., & McWilliams, K. A. (2021). On optimum solar wind-magnetosphere coupling functions for transpolar voltage and planetary geomagnetic activity. *Journal of Geophysical Research: Space Physics*, *126*(12), e2021JA029946.

Milan, S., Gosling, J., & Hubert, B. (2012). Relationship between interplanetary parameters and the magnetopause reconnection rate quantified from observations of the expanding polar cap. *Journal of Geophysical Research: Space Physics*, *117*(A3).

Milan, S., Provan, G., & Hubert, B. (2007). Magnetic flux transport in the dungey cycle: A survey of dayside and nightside reconnection rates. *Journal of Geophysical Research: Space Physics*, *112*(A1).

Pettigrew, E., Shepherd, S., & Ruohoniemi, J. (2010). Climatological patterns of high-latitude convection in the northern and southern hemispheres: Dipole tilt dependencies and interhemispheric comparisons. *Journal of Geophysical Research: Space Physics*, *115*(A7).

Qian, L., Burns, A. G., Emery, B. A., Foster, B., Lu, G., Maute, A., ... Wang, W. (2014). The ncar tie-gcm: A community model of the coupled thermosphere/ionosphere system. *Modeling the ionosphere-thermosphere system*, *201*, 73–83.

Reiff, P., Spiro, R., Wolf, R., Kamide, Y., & King, J. (1985). Comparison of polar cap potential drops estimated from solar wind and ground magnetometer data: Cdaw 6. *Journal of Geophysical Research: Space Physics*, *90*(A2), 1318–1324.

Reiff, P. H., Spiro, R. W., & Hill, T. (1981). Dependence of polar cap potential drop on interplanetary parameters. *Journal of Geophysical Research: Space Physics*, *86*(A9), 7639–7648.

Rich, F., & Maynard, N. (1989). Consequences of using simple analytical functions for the high-latitude convection electric field. *Journal of Geophysical Research: Space Physics*, *94*(A4), 3687–3701.

Richmond, A., & Kamide, Y. (1988). Mapping electrodynamic features of the high-latitude ionosphere from localized observations: Technique. *Journal of Geophysical Research: Space Physics*, *93*(A6), 5741–5759.

Ridley, A., & Kihn, E. (2004). Polar cap index comparisons with amie cross polar cap potential, electric field, and polar cap area. *Geophysical research letters*, *31*(7).

Ruohoniemi, J., & Baker, K. (1998). Large-scale imaging of high-latitude convection with super dual auroral radar network hf radar observations. *Journal of Geophysical Research: Space Physics*, *103*(A9), 20797–20811.

Ruohoniemi, J., & Greenwald, R. (1996). Statistical patterns of high-latitude convection obtained from goose bay hf radar observations. *Journal of Geophysical Research: Space Physics*, *101*(A10), 21743–21763.

Shepherd, S. (2014). Altitude-adjusted corrected geomagnetic coordinates: Definition and functional approximations. *Journal of Geophysical Research: Space Physics*, *119*(9), 7501–7521.

Shepherd, S., Greenwald, R., & Ruohoniemi, J. (2002). Cross polar cap potentials measured with super dual auroral radar network during quasi-steady solar wind and interplanetary magnetic field conditions. *Journal of Geophysical Research: Space Physics*, *107*(A7), SMP–5.

Shepherd, S. G. (2007). Polar cap potential saturation: Observations, theory, and modeling. *Journal of Atmospheric and Solar-Terrestrial Physics*, *69*(3), 234–248.

Shue, J.-H., Chao, J., Fu, H., Russell, C., Song, P., Khurana, K., & Singer, H. (1997). A new functional form to study the solar wind control of the magnetopause size and shape. *Journal of Geophysical Research: Space Physics*, *102*(A5), 9497–9511.

Siscoe, G., & Huang, T. (1985). Polar cap inflation and deflation. *Journal of Geophysical Research: Space Physics*, *90*(A1), 543–547.

Siscoe, G. L. (1982). Polar cap size and potential: A predicted relationship. *Geophysical Research Letters*, *9*(6), 672–675.

SuperDARN Data Analysis Working Group, Schmidt, M., Bland, E., Thomas, E.,

Burrell, A., Coco, I., . . . Walach, M.-T. (2021, August). *Superdarn/rst: Rst 4.6.* Zenodo. Retrieved from `https://doi.org/10.5281/zenodo.5156752` doi: 10.5281/zenodo.5156752

Thomas, E. G., & Shepherd, S. G. (2018). Statistical patterns of ionospheric convection derived from mid-latitude, high-latitude, and polar superdarn hf radar observations. *Journal of Geophysical Research: Space Physics*, *123*(4), 3196–3216.

Volland, H. (1975). Models of the global electric fields within the magnetosphere. *Ann. Geophys.*, *31*, 159–173.

Walach, M.-T., & Grocott, A. (2019). Superdarn observations during geomagnetic storms, geomagnetically active times, and enhanced solar wind driving. *Journal of Geophysical Research: Space Physics*, *124*(7), 5828–5847.

Walach, M.-T., & Grocott, A. (2022). Modelling the time-variability of the ionospheric electric field (tivie). *Journal of Space Weather and Space Climate (Submitted)*.

Walach, M.-T., Grocott, A., & Milan, S. E. (2021). Average ionospheric electric field morphologies during geomagnetic storm phases. *Journal of Geophysical Research: Space Physics*, *126*(4), e2020JA028512.

Walach, M.-T., Grocott, A., Staples, F., & Thomas, E. G. (2022). Super dual auroral radar network expansion and its influence on the derived ionospheric convection pattern. *Journal of Geophysical Research: Space Physics*, *127*(2), e2021JA029559.

Weimer, D. (1995). Models of high-latitude electric potentials derived with a least error fit of spherical harmonic coefficients. *Journal of Geophysical Research: Space Physics*, *100*(A10), 19595–19607.

Weimer, D. (1996). A flexible, imf dependent model of high-latitude electric potentials having "space weather" applications. *Geophysical Research Letters*, *23*(18), 2549–2552.

Weimer, D. (2001). An improved model of ionospheric electric potentials including substorm perturbations and application to the geospace environment modeling november 24, 1996, event. *Journal of Geophysical Research: Space Physics*, *106*(A1), 407–416.

Weimer, D. (2005). Improved ionospheric electrodynamic models and application to calculating joule heating rates. *Journal of Geophysical Research: Space Physics*, *110*(A5).

Weimer, D. (2019, January). *Weimer 2005 ionospheric electric potential model for IDL.* Zenodo. Retrieved from `https://doi.org/10.5281/zenodo.2530324` doi: 10.5281/zenodo.2530324
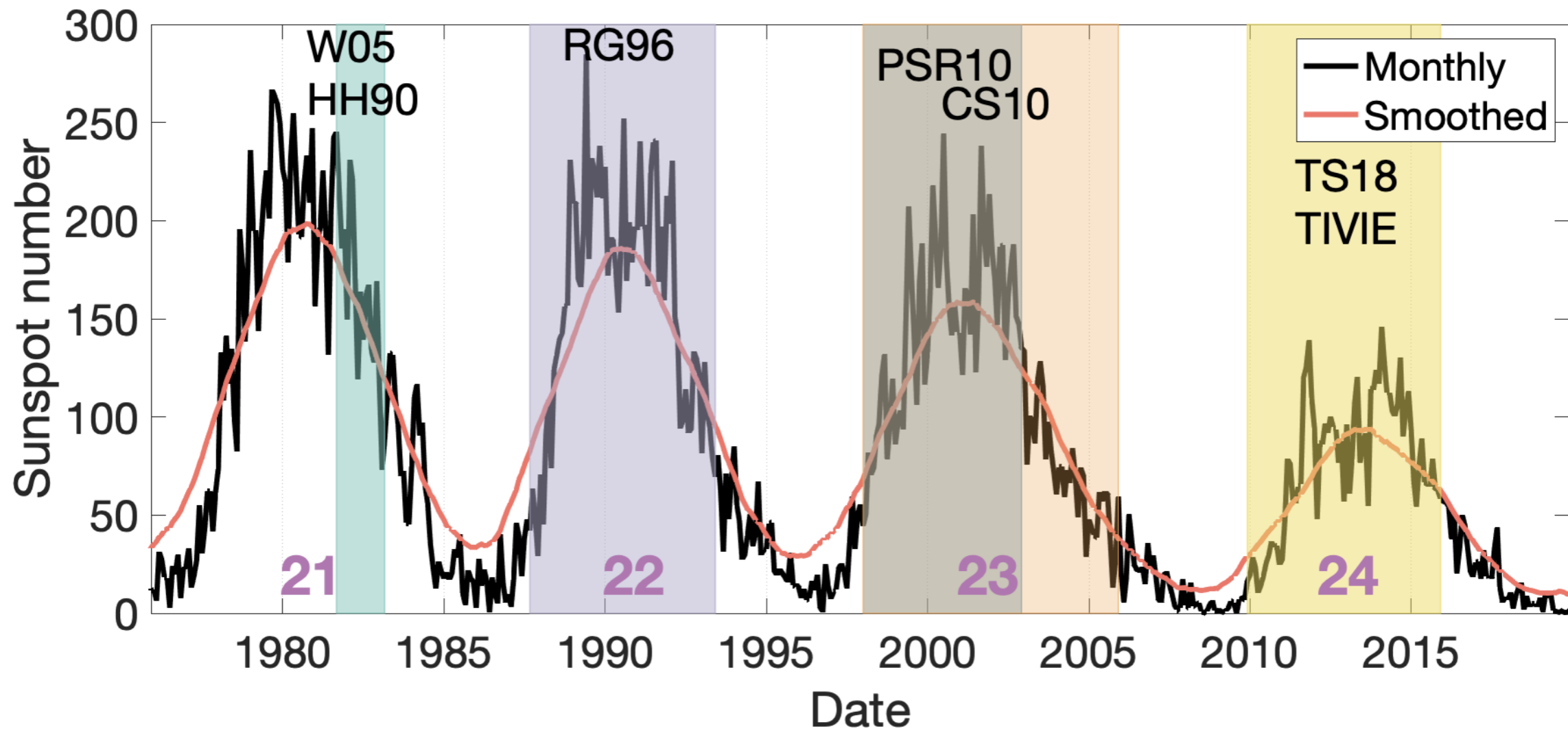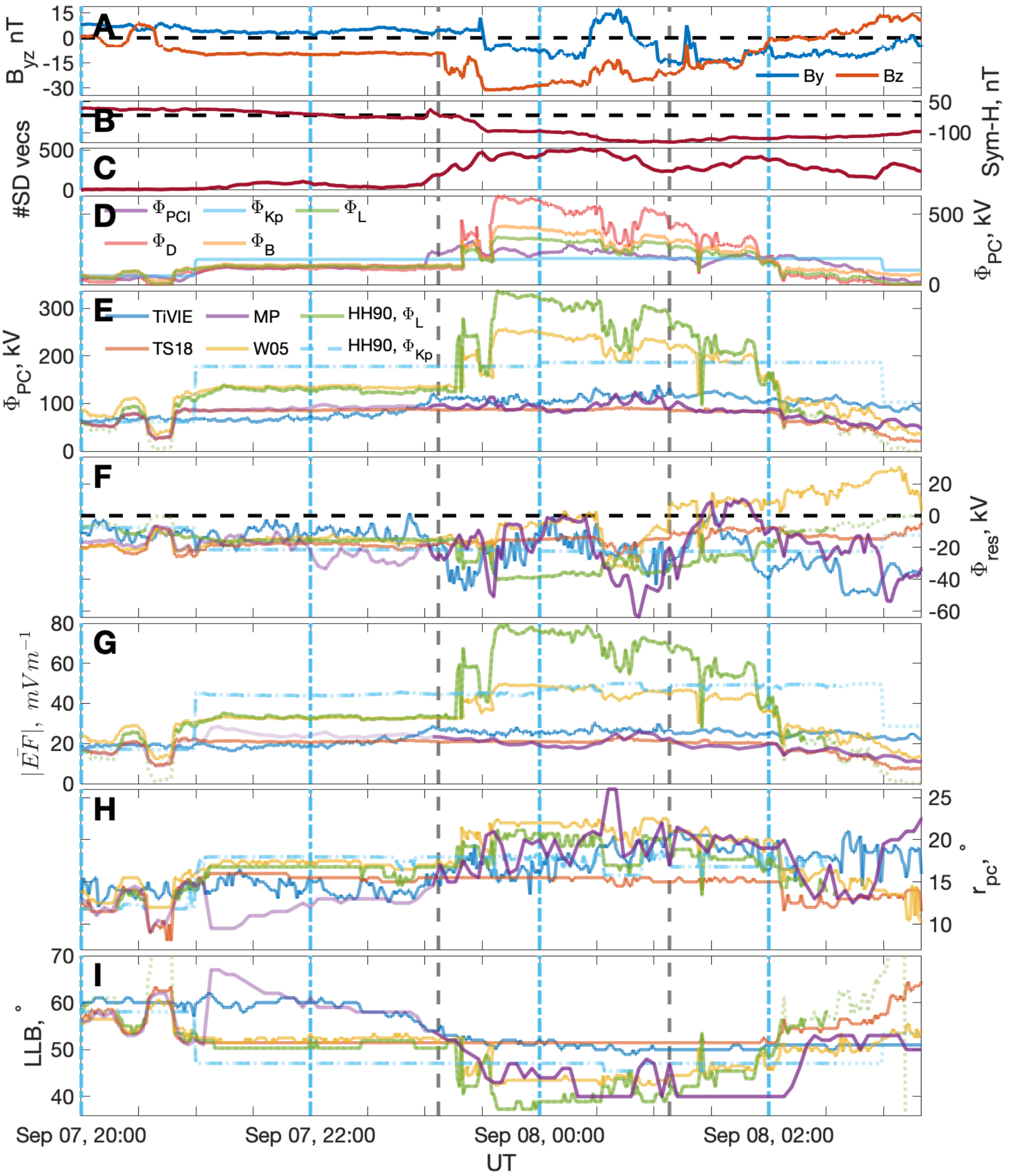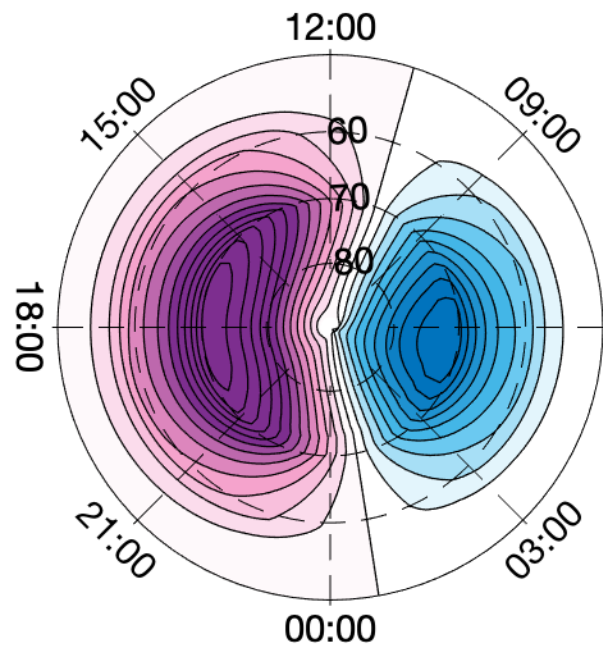
Figure 1.

Figure 2.

Figure 3.

	W05	HH90, Φ_L	HH90, Φ_{Kp}	TS18	Map potential	TiVIE

07 September 2017, 20:00, B_y=7.7nT, B_z=-1.3nT, V=497km/s, Kp=2.7, Sym-H=18nT, #SD vecs=2

Φ_{Min}=-53.1 kV, Φ_{Max}=32.3 kV, Φ_{pc}=85.4 kV

Φ_{Min}=-33.8 kV, Φ_{Max}=26.4 kV, Φ_{pc}=60.2 kV

Φ_{Min}=-34.6 kV, Φ_{Max}=27 kV, Φ_{pc}=61.5 kV

Φ_{Min}=-40.1 kV, Φ_{Max}=20.2 kV, Φ_{pc}=60.4 kV

Φ_{Min}=-39 kV, Φ_{Max}=22.1 kV, Φ_{pc}=61 kV

Φ_{Min}=-37 kV, Φ_{Max}=24.6 kV, Φ_{pc}=61.6 kV

07 September 2017, 22:00, B_y=3.1nT, B_z=-9.2nT, V=466km/s, Kp=7.7, Sym-H=-11nT, #SD vecs=92

Φ_{Min}=-72.5 kV, Φ_{Max}=58.7 kV, Φ_{pc}=131 kV

Φ_{Min}=-69.6 kV, Φ_{Max}=54.6 kV, Φ_{pc}=124 kV

Φ_{Min}=-99.6 kV, Φ_{Max}=78.3 kV, Φ_{pc}=178 kV

Φ_{Min}=-50 kV, Φ_{Max}=33.3 kV, Φ_{pc}=83.3 kV

Φ_{Min}=-56.3 kV, Φ_{Max}=34 kV, Φ_{pc}=90.3 kV

Φ_{Min}=-43.2 kV, Φ_{Max}=32.2 kV, Φ_{pc}=75.3 kV

08 September 2017, 00:00, B_y=-7.3nT, B_z=-29nT, V=690km/s, Kp=8, Sym-H=-92nT, #SD vecs=438

Φ_{Min}=-127 kV, Φ_{Max}=122 kV, Φ_{pc}=249 kV

Φ_{Min}=-180 kV, Φ_{Max}=141 kV, Φ_{pc}=321 kV

Φ_{Min}=-104 kV, Φ_{Max}=81.9 kV, Φ_{pc}=186 kV

Φ_{Min}=-51 kV, Φ_{Max}=36.1 kV, Φ_{pc}=87 kV

Φ_{Min}=-54.2 kV, Φ_{Max}=39 kV, Φ_{pc}=93.2 kV

Φ_{Min}=-59.4 kV, Φ_{Max}=42.7 kV, Φ_{pc}=102 kV

08 September 2017, 02:00, B_y=-9nT, B_z=-7.7nT, V=780km/s, Kp=8, Sym-H=-128nT, #SD vecs=373

Φ_{Min}=-73.1 kV, Φ_{Max}=81.7 kV, Φ_{pc}=155 kV

Φ_{Min}=-91.5 kV, Φ_{Max}=71.9 kV, Φ_{pc}=163 kV

Φ_{Min}=-104 kV, Φ_{Max}=81.9 kV, Φ_{pc}=186 kV

Φ_{Min}=-45.1 kV, Φ_{Max}=37.8 kV, Φ_{pc}=83 kV

Φ_{Min}=-49.5 kV, Φ_{Max}=39.6 kV, Φ_{pc}=89.1 kV

Φ_{Min}=-71 kV, Φ_{Max}=39 kV, Φ_{pc}=110 kV

Electric potential, kV

Figure 4.

a) Φ_{PCI} **b)** Φ_{D} **c)** Φ_{Kp} **d)** Φ_{L} **e)** Φ_{Weimer} **f)** Φ_{TS18}

08 September 2017, 00:00, B_y=-7.3nT, B_z=-29nT, V=690km/s, Kp=8, SYM/H=-92nT, #vecs=219

Φ_{Min}=-127 kV Φ_{pc}=226 kV
Φ_{Max}=99.4 kV

Φ_{Min}=-330 kV Φ_{pc}=589 kV
Φ_{Max}=259 kV

Φ_{Min}=-104 kV Φ_{pc}=186 kV
Φ_{Max}=81.9 kV

Φ_{Min}=-180 kV Φ_{pc}=321 kV
Φ_{Max}=141 kV

Φ_{Min}=-139 kV Φ_{pc}=249 kV
Φ_{Max}=110 kV

Φ_{Min}=-48.7 kV Φ_{pc}=86.9 kV
Φ_{Max}=38.3 kV

Electric potential, kV

Figure 5.

Dusk -> Dawn Directed Electric field Vectors
Dusk -> Dawn Directed Electric field Vectors

A) B_{yz}
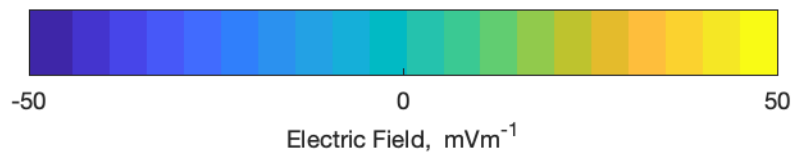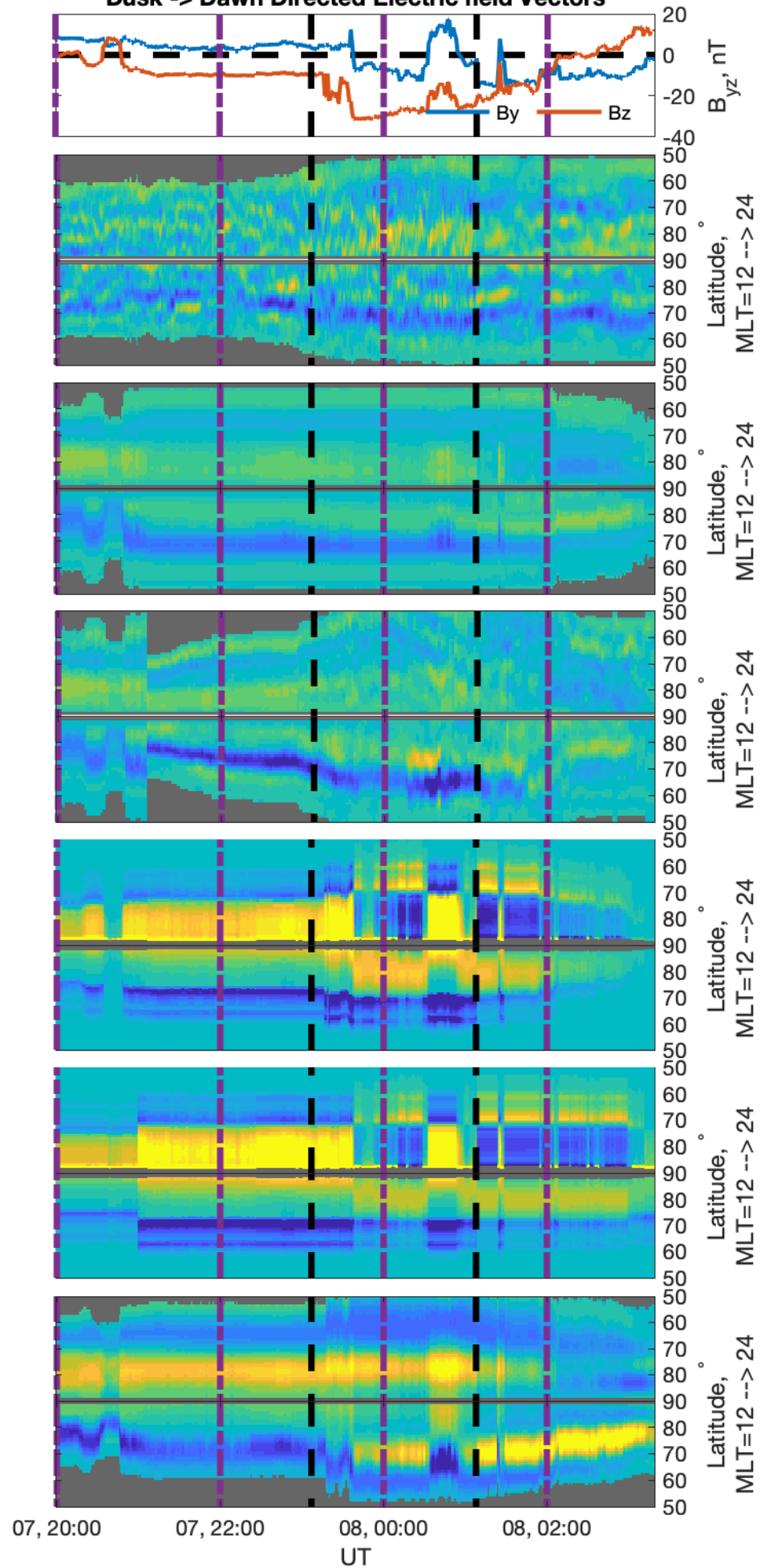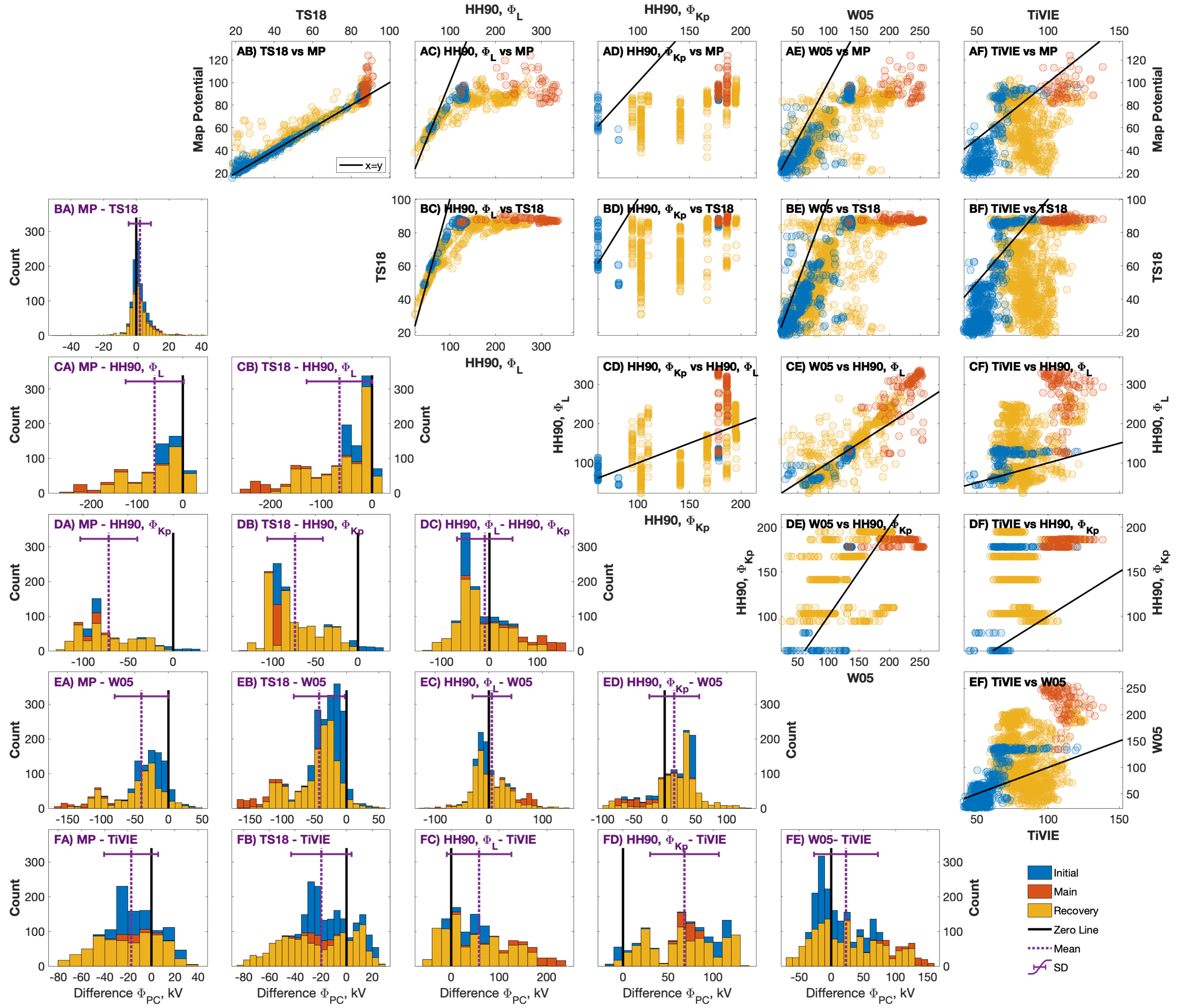
B) TiVIE

C) TS18

D) Map Potential

E) HH90, Φ_L

F) HH90, Φ_{Kp}

G) W05

Electric Field, mVm⁻¹

Figure 6.

Φ_{PC}, kV

Figure 7.

LLB, °